Large Population of ALMA Galaxies at $z > 6$ with Very High [O III] 88 μm to [C II] 158 μm Flux Ratios: Evidence of Extremely High Ionization Parameter or PDR Deficit?

Yuichi Harikane[1,2] , Masami Ouchi[1,3,4] , Akio K. Inoue[5,6], Yoshiki Matsuoka[7], Yoichi Tamura[8] , Tom Bakx[1,8],
Seiji Fujimoto[1,6] , Kana Moriwaki[9], Yoshiaki Ono[3], Tohru Nagao[7] , Ken-ichi Tadaki[1] , Takashi Kojima[3,9] ,
Takatoshi Shibuya[10], Eiichi Egami[11], Andrea Ferrara[12] , Simona Gallerani[12], Takuya Hashimoto[6] , Kotaro Kohno[13] ,
Yuichi Matsuda[1,14] , Hiroshi Matsuo[1,14], Andrea Pallottini[12,15], Yuma Sugahara[1,3,6,9] , and Livia Vallini[16]
[1] National Astronomical Observatory of Japan, 2-21-1 Osawa, Mitaka, Tokyo 181-8588, Japan; yuichi.harikane@nao.ac.jp
[2] Department of Physics and Astronomy, University College London, Gower Street, London WC1E 6BT, UK
[3] Institute for Cosmic Ray Research, The University of Tokyo, 5-1-5 Kashiwanoha, Kashiwa, Chiba 277-8582, Japan
[4] Kavli Institute for the Physics and Mathematics of the Universe (WPI), University of Tokyo, Kashiwa 277-8583, Japan
[5] Department of Physics, School of Advanced Science and Engineering, Waseda University, 3-4-1 Okubo, Shinjuku, Tokyo 169-8555, Japan
[6] Waseda Research Institute for Science and Engineering, 3-4-1 Okubo, Shinjuku, Tokyo 169-8555, Japan
[7] Research Center for Space and Cosmic Evolution, Ehime University, Bunkyo-cho, Matsuyama, Ehime 790-8577, Japan
[8] Division of Particle and Astrophysical Science, Graduate School of Science, Nagoya University, Nagoya 464-8602, Japan
[9] Department of Physics, Graduate School of Science, The University of Tokyo, 7-3-1 Hongo, Bunkyo, Tokyo, 113-0033, Japan
[10] Kitami Institute of Technology, 165 Koen-cho, Kitami, Hokkaido 090-8507, Japan
[11] Steward Observatory, University of Arizona, 933 N. Cherry Avenue, Tucson, AZ 85721, USA
[12] Scuola Normale Superiore, Piazza dei Cavalieri 7, I-50126 Pisa, Italy
[13] Institute of Astronomy, Graduate School of Science, The University of Tokyo, 2-21-1 Osawa, Mitaka, Tokyo 181-0015, Japan
[14] Department of Astronomical Science, The Graduate University for Advanced Studies (SOKENDAI), 2-21-1 Osawa, Mitaka, Tokyo 181-8588, Japan
[15] Centro Fermi, Museo Storico della Fisica e Centro Studi e Ricerche "Enrico Fermi," Piazza del Viminale 1, Roma, I-00184, Italy
[16] Leiden Observatory, Leiden University, PO Box 9500, 2300 RA Leiden, The Netherlands
Received 2019 October 24; revised 2020 May 14; accepted 2020 May 18; published 2020 June 17

Abstract

We present our new Atacama Large Millimeter/Submillimeter Array (ALMA) observations targeting [O III]88 μm, [C II]158 μm, [N II]122 μm, and dust-continuum emission for three Lyman break galaxies at $z = 6.0293$–6.2037, identified in the Subaru/Hyper Suprime-Cam survey. We clearly detect [O III] and [C II] lines from all of the galaxies at 4.3–11.8σ levels, and identify multi-band dust-continuum emission in two of the three galaxies, allowing us to estimate infrared luminosities and dust temperatures simultaneously. In conjunction with previous ALMA observations for six galaxies at $z > 6$, we confirm that all the nine $z = 6$–9 galaxies have high [O III]/[C II] ratios of $L_{\rm [O III]}/L_{\rm [C II]} \sim 3$–$20$, ~ 10 times higher than $z \sim 0$ galaxies. We also find a positive correlation between the [O III]/[C II] ratio and the Lyα equivalent width (EW) at the $\sim 90\%$ significance level. We carefully investigate physical origins of the high [O III]/[C II] ratios at $z = 6$–9 using Cloudy, and find that high density of the interstellar medium, low C/O abundance ratio, and the cosmic microwave background attenuation are responsible to only a part of the $z = 6$–9 galaxies. Instead, the observed high [O III]/[C II] ratios are explained by 10–100 times higher ionization parameters or low photodissociation region (PDR) covering fractions of 0%–10%, both of which are consistent with our [N II] observations. The latter scenario can be reproduced with a density-bounded nebula with PDR deficit, which would enhance the Lyα, Lyman continuum, and C$^+$ ionizing photons escape from galaxies, consistent with the [O III]/[C II]-Lyα EW correlation we find.

Unified Astronomy Thesaurus concepts: Galaxy evolution (594)

1. Introduction

Understanding properties of the interstellar medium (ISM) is important for galaxy formation. The metallicity in the gas phase (hereafter metallicity) can be a tracer of the past star formation history including gas inflow and outflow, because heavy elements produced in stars through star formation activities are returned into the ISM (e.g., Maiolino & Mannucci 2019). The ionization parameter, $q_{\rm ion}$, is also an important quantity that characterizes the ionization state in the ISM, defined by

$$q_{\rm ion} = \frac{Q_0}{4\pi R_{\rm s}^2 n_{\rm H}}, \qquad (1)$$

in units of cm s^{-1}, where Q_0 and $n_{\rm H}$ are the hydrogen-ionizing photon production rate and hydrogen density, respectively. $R_{\rm s}$

is the Strömgren radius defined by

$$Q_0 = \frac{4}{3} R_{\rm s}^3 n_{\rm H}^2 \alpha_{\rm B} \epsilon, \qquad (2)$$

where $\alpha_{\rm B}$ and ϵ are the case B recombination rate and the volume filling factor, respectively. The ionization parameter is sometimes normalized by the light speed c,

$$U_{\rm ion} = \frac{q_{\rm ion}}{c}. \qquad (3)$$

The ionization parameter can be also related to the escape fraction of ionizing photons that is key for cosmic reionization physics (e.g., Nakajima & Ouchi 2014).

Nebular emission lines are powerful tools to investigate the ISM properties of galaxies. Spectroscopic observations for rest-frame optical lines reveal that galaxies at $z \sim 2-3$ have lower

metallicities (e.g., Maiolino et al. 2008), higher ionization parameters (e.g., Nakajima & Ouchi 2014), and higher densities (e.g., Shimakawa et al. 2015; Sanders et al. 2016; Kashino et al. 2017), compared to local galaxies. However, it is difficult to study the ISM properties of higher redshift galaxies, especially at $z > 5$, because commonly used rest-frame optical-emission lines, such as $H\alpha$, $H\beta$, [O III]$\lambda\lambda$4959,5007, and [O II] $\lambda\lambda$3726,3729 are redshifted out from the atmospheric window in the near-infrared, and ground-based telescopes cannot observe these lines. Although rest-frame ultraviolet (UV) metal lines such as [C III]1907 and [C III]1909 are used to study $z \sim 6-8$ galaxies (e.g., Stark et al. 2015a, 2015b, 2017), these lines are typically weak and not always detected (e.g., Mainali et al. 2018; Shibuya et al. 2018). Broad-band photometry with the Spitzer Space Telescope gives some constraints on the rest-frame optical lines at $z > 4$ (e.g., Faisst et al. 2016; Roberts-Borsani et al. 2016; Harikane et al. 2018b), but this method can be used only for galaxies in limited redshift ranges. Spectroscopy for strong nebular lines is important for understanding the ISM properties of high-redshift galaxies, but we need to wait for the launch of the James Webb Space Telescope for the rest-frame optical lines of $z > 5$ galaxies.

Far-infrared (FIR) emission lines studied with Atacama Large Millimeter/Submillimeter Array (ALMA) are alternative tools to study the ISM of high-redshift galaxies. Previous ALMA observations report surprisingly weak [C II]158 μm emission in Lyα emitters (LAEs) at $z \sim 6-7$ compared to local galaxies with similar star formation rates (SFRs), known as the [C II] deficit (e.g., Ota et al. 2014; Schaerer et al. 2015; Knudsen et al. 2016). On the other hand, some Lyman break galaxies (LBGs) detected by ALMA at $z \sim 5-7$ have [C II] luminosity to SFR ratios ($L_{[CII]}$/SFR) comparable to local galaxies (e.g., Capak et al. 2015; Pentericci et al. 2016). This difference of the $L_{[CII]}$/SFR ratio may include key information of an evolution of the ISM properties from low redshift to high redshift. Based on these observations, Harikane et al. (2018b) have identified an anticorrelation between $L_{[CII]}$/SFR and the Lyα equivalent width (EW), $EW^0_{Ly\alpha}$, which is also reported in Carniani et al. (2018a) and Matthee et al. (2019). Since the Lyα EW correlates well with the Lyα photon escape fraction (e.g., Sobral et al. 2017; Harikane et al. 2018b; Sobral & Matthee 2019), this anticorrelation indicates that the strength of the [C II] emission is related to the Lyα photon escape from galaxies.

The [O III]88 μm emission line is predicted to be detectable from $z > 6$ galaxies with ALMA (Inoue et al. 2014), and is indeed detected (Inoue et al. 2016; Laporte et al. 2017a; Carniani et al. 2017; Hashimoto et al. 2018, 2019a; Tamura et al. 2019), including the most distant emission line galaxy at $z = 9.1096$ (Hashimoto et al. 2018). Given the high success rate of ALMA [O III] observations, the [O III] line is one of the most useful tracers for ISM properties at $z \gtrsim 6$. Since [O III] has an ionization potential (35.1 eV) higher than [C II] (11.3 eV), the [O III]/[C II] ratio is useful to investigate ionization state. However, the number of galaxies with both [O III] and [C II] observations is limited; for LBGs and LAEs currently only six galaxies are reported (Inoue et al. 2016; Carniani et al. 2017; Laporte et al. 2017a, 2019; Hashimoto et al. 2018, 2019a; Tamura et al. 2019; Bakx et al. 2020).

ALMA observations have also begun to reveal the complex nature of dust-obscured star formation in the high-redshift universe. Dust obscuration is usually quantified by the IR to UV luminosity ratio (IRX $= L_{IR}/L_{UV}$) as a function of the UV slope β_{UV} (IRX–β_{UV}). Local starburst galaxies show a correlation between IRX and β_{UV} (e.g., Meurer et al. 1999; Calzetti et al. 2000), which is known as the Calzetti IRX–β_{UV} relation. Takeuchi et al. (2012) modified the Calzetti IRX–β_{UV} relation considering the aperture effect in the photometry in UV. The Small Magellanic Cloud (SMC) shows lower IRX values than the Calzetti relation, known as the SMC IRX–β_{UV} relation (e.g., Pettini et al. 1998). Herschel and ALMA observations reveal that $z \sim 2-5$ galaxies follow the Calzetti or SMC IRX–β_{UV} curves (e.g., Fudamoto et al. 2017; Koprowski et al. 2018; McLure et al. 2018; Reddy et al. 2018). On the other hand at $z > 5$, some galaxies show IRX values significantly lower than these relations (e.g., Capak et al. 2015; Bouwens et al. 2016; Barisic et al. 2017), implying significant evolution of dust properties from $z \sim 0$ to $z > 5$ (see also Gallerani et al. 2010). There are several possibilities for the physical origin of the low IRX values in high-redshift galaxies. One of the most important caveats is that dust temperatures are not determined in most of the galaxies at $z > 5$, as discussed in several studies (e.g., Bouwens et al. 2016; Faisst et al. 2017; Behrens et al. 2018). Since these galaxies are often observed in one single FIR band, the dust temperature (T_{dust}) is usually assumed to match local galaxy values to derive the IR luminosity. However, Faisst et al. (2017) point out that dust temperatures of high-redshift galaxies could be significantly higher, which increases L_{IR} up to 0.6 dex with the higher dust temperature by $\Delta T_{dust} = +40$ K, possibly resolving the tension between the models and observations (see also Hashimoto et al. 2019a; Laporte et al. 2019; Tamura et al. 2019). Additionally, using cosmological zoom-in simulations (Pallottini et al. 2017a), Behrens et al. (2018) shows that 20% of the dust mass can be responsible for up to 80% of the IR luminosity, because of the high ($\sim$70 K) dust temperature due to the compactness and intense radiation field typical of high-redshift galaxies. Thus we need to simultaneously constrain dust temperatures and IR luminosities with multi-band dust-continuum observations.

In this study, we present our new ALMA observations targeting [O III]88 μm, [C II]158 μm, [N II]122 μm, and multi-band dust-continuum emission in three LBGs at $z \sim 6$ that are identified in the Subaru/Hyper Suprime-Cam survey (Aihara et al. 2018). Optical spectroscopic observations have already detected Lyα emission lines in these galaxies (Matsuoka et al. 2018b). In conjunction with previous ALMA observations for $z > 5$ galaxies and Cloudy model calculations, we study ISM properties of the high-redshift galaxies.

This paper is organized as follows. In Section 2, we describe our targets and optical spectroscopy already conducted. Our ALMA observations are presented in Section 3. We present our results for the FIR emission lines and dust-continuum emission in Sections 4 and 5, respectively. In Section 6, we discuss our results based on model calculations by Cloudy. Section 7 summarizes our findings. Throughout this paper, we use the recent Planck cosmological parameter sets constrained with the temperature power spectrum, temperature-polarization cross spectrum, polarization power spectrum, low-l polarization, CMB lensing, and external data (TT, TE, EE+lowP+lensing +ext result; Planck Collaboration et al. 2016): $\Omega_m = 0.3089$, $\Omega_\Lambda = 0.6911$, $\Omega_b = 0.049$, and $h = 0.6774$. We assume a Chabrier (2003) initial mass function (IMF) with lower and upper mass cutoffs of 0.1 $M_\odot$ and 100 $M_\odot$, respectively. All

Table 1
Summary of Observational Results of Our Targets

	J1211-0118	J0235-0532	J0217-0208
R.A.	12:11:37.112	02:35:42.412	02:17:21.603
Decl.	−01:18:16.500	−05:32:41.623	−02:08:52.778
M_{UV} [AB mag]	−22.8	−22.8	−23.3
L_{UV} ($L_\odot$)	2.7×10^{11}	2.9×10^{11}	4.3×10^{11}
$EW^0_{Ly\alpha}$ (Å)	6.9 ± 0.8	41 ± 2	15 ± 1
β_{UV}	-2.0 ± 0.5	-2.6 ± 0.6	-0.1 ± 0.5
$z_{[O III]}$	6.0295 ± 0.0009	6.0906 ± 0.0009	6.2044 ± 0.0013
$z_{[C II]}$	6.0291 ± 0.0008	6.0894 ± 0.0010	6.2033 ± 0.0009
z_{sys}	6.0293 ± 0.0002	6.0901 ± 0.0006	6.2037 ± 0.0005
$z_{Ly\alpha}$	6.0339 ± 0.0008	6.0918 ± 0.0002	6.2046 ± 0.0006
$\Delta v_{Ly\alpha}$ (km s^{-1})	196 ± 35	71 ± 26	37 ± 32
[O III] integrated flux (Jy km s^{-1})	2.69 ± 0.40 (6.7σ)	2.10 ± 0.18 (11.8σ)	4.57 ± 1.06 (4.3σ)
[C II] integrated flux (Jy km s^{-1})	1.42 ± 0.15 (9.5σ)	0.43 ± 0.07 (5.9σ)	1.36 ± 0.20 (6.7σ)
[N II] integrated flux (Jy km s^{-1})	<0.66 (3σ)	<0.90 (3σ)	<0.45 (3σ)
FWHM$_{[O III]}$ (km s^{-1})	194 ± 123	389 ± 117	374 ± 162
FWHM$_{[C II]}$ (km s^{-1})	170 ± 98	270 ± 135	316 ± 117
$L_{[O III]}$ ($L_\odot$)	$(4.8 \pm 0.7) \times 10^9$	$(3.8 \pm 0.3) \times 10^9$	$(8.5 \pm 2.0) \times 10^9$
$L_{[C II]}$ ($L_\odot$)	$(1.4 \pm 0.1) \times 10^9$	$(4.3 \pm 0.7) \times 10^8$	$(1.4 \pm 0.2) \times 10^9$
$L_{[NII]}$ ($L_\odot$)	$<8.3 \times 10^8$	$<1.2 \times 10^9$	$<6.2 \times 10^8$
$L_{[O III]}/L_{[C II]}$	3.4 ± 0.6	8.9 ± 1.7	6.0 ± 1.7
$L_{[O III]}/L_{[N II]}$	>5.8	>3.2	>13.8
$S_{\nu,160}$ (μJy)	220 ± 51 (4.3σ)	<101(3σ)	239 ± 79 (3.0σ)
$S_{\nu,120}$ (μJy)	382 ± 72 (5.3σ)	<162 (3σ)	310 ± 43 (7.1σ)
$S_{\nu,90}$ (μJy)	<826 (3σ)	<394 (3σ)	<606 (3σ)
L_{IR} ($L_\odot$)	$3.2^{+18.7}_{-1.7} \times 10^{11}$	$<2.5 \times 10^{11}$ (3σ)	$1.4^{+2.5}_{-0.3} \times 10^{11}$
T_{dust} (K)	38^{+34}_{-12}	...	25^{+19}_{-5}
M_{dust} ($M_\odot$)	$3.0^{+10.5}_{-2.3} \times 10^7$	$<6.9 \times 10^6$ (3σ)	$1.9^{+73.5}_{-1.6} \times 10^8$
SFR$_{tot}$ ($M_\odot$ yr^{-1})	86	54	96
SFR$_{UV}$ ($M_\odot$ yr^{-1})	51	54	80
SFR$_{IR}$ ($M_\odot$ yr^{-1})	34	<27	16

magnitudes are in the AB system (Oke & Gunn 1983), and are corrected for Galactic extinction (Schlegel et al. 1998).

2. Target Selection

We select targets for our ALMA observations from the Subaru/Hyper Suprime-Cam Subaru strategic program (HSC-SSP) survey data sets (Aihara et al. 2018). The Subaru/HSC survey is a photometric survey with optical broad-band filters *grizy* and several narrow-band filters. The HSC survey has three layers, UltraDeep, Deep, and Wide, with different combinations of area and depth (see Aihara et al. 2018 for details). LBGs at $z \sim 4-7$ are selected from the HSC data sets with the dropout selection technique (Harikane et al. 2018a; Matsuoka et al. 2016, 2018a, 2018b, 2019; Ono et al. 2018; Toshikawa et al. 2018), and some of the LBGs are spectroscopically confirmed (Matsuoka et al. 2016, 2018a, 2018b, 2019; Ono et al. 2018).

As the first step to understand ISM properties of high-redshift galaxies, we select three luminous LBGs, J1211-0118, J0235-0532, and J0217-0208, as targets for ALMA observations (Table 1). All targets are spectroscopically confirmed with Lyα in the SHELLQs project (Matsuoka et al. 2018b), and their redshifts, $6.0 < z_{Ly\alpha} < 6.3$, are suitable for ALMA Band 6, 7, and 8 observations targeting [C II]158 μm, [N II]122 μm, and

[O III]88 μm, respectively. J1211-0118 shows a weak Lyα emission line with a rest-frame Lyα EW of $EW^0_{Ly\alpha} = 6.9 \pm 0.8$ Å. J0235-0532 and J0217-0208 show strong Lyα emission lines with $EW^0_{Ly\alpha} = 41 \pm 2$ and 15 ± 1 Å, respectively. The broad dynamical range of the Lyα EW makes our targets representative in terms of Lyα emission. The spectroscopic data also indicate that the targets do not have broad Lyα (>400 km s^{-1}) nor Nv emission lines. J0235-0532 and J0217-0208 exhibit large Lyα luminosities of $L_{Ly\alpha} > 10^{43}$ erg s^{-1}, powerful enough to be associated with active galactic nuclei (AGNs) as suggested by Konno et al. (2016) at $z \sim 2$, while a spectroscopic study by Shibuya et al. (2018) do not find signatures of AGN activity (e.g., C IV emission) in such luminous LAEs at $z \sim 6-7$. NIR spectroscopy is important for understanding possible AGN activities in J0235-0532 and J0217-0208.

3. ALMA Observations and Data Reduction

The three LBGs at $z \sim 6$ were observed during ALMA cycle 5 (ID: #2017.1.00508.S, PI: Y. Harikane) at Bands 6, 7, and 8 for [C II]158 μm, [N II]122 μm, and [O III]88 μm, between 2018 April 3 and 2018 June 22. The antenna configurations were C43-1, C43-2, and C43-3, achieving the beam sizes of

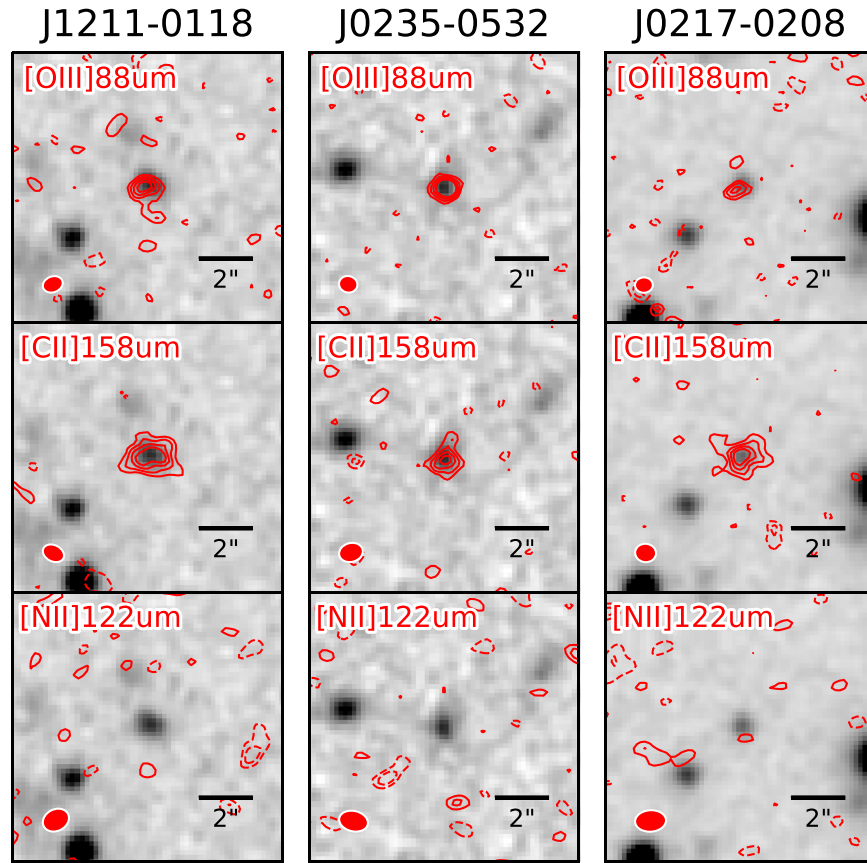## J1211-0118   J0235-0532   J0217-0208

Figure 1. [O III]88 μm, [C II]158 μm, and [N II]122 μm emission of our targets after continuum subtraction. The red contours are [O III], [C II], and [N II] emission, and are drawn at 1σ intervals from $\pm 2\sigma$ to $\pm 5\sigma$. Positive and negative contours are shown by the solid and dashed lines, respectively. The backgrounds are rest-UV and Lyα image (the Subaru/HSC z-band) whose typical seeing size is 0$.\!\!''$7. The images are 10$''$ × 10$''$, and the red ellipses at the lower left corner indicate the synthesized beam sizes of ALMA.

$\sim$0$.\!\!''$6–1$.\!\!''$1 and the maximum recoverable scales of 6–7$''$. We used four spectral windows (SPWs) with 1.875 GHz bandwidths in the Frequency Division Mode and the total bandwidth of 7.5 GHz. The velocity resolution was set to $\sim$3–5 km s^{-1}. One of the SPWs was centered on the [C II], [N II], or [O III] line frequency expected from the redshift of the Lyα emission.

The data were reduced and calibrated using the Common Astronomy Software (CASA; McMullin et al. 2007) pipeline version 5.1.1 in the general manner with scripts provided by the ALMA observatory. Using the task CLEAN, we produced images and cubes with the natural weighting without taper to maximize point-source sensitivities. To generate a pure dust-continuum image, we collapsed all SPWs except for one SPW where the [C II], [N II], or [O III] line is located, i.e., the continuum is taken at $\gtrsim$600 km s^{-1} from the line center. To create a pure line image, we subtracted continuum using the off-line channels in the line cube with the CASA task uvcontsub.

4. FIR Emission Lines

4.1. Line Detections and Upper Limits

Figure 1 displays the [O III]88 μm, [C II]158 μm, and [N II] 122 μm emission lines of our three targets. These moment 0 maps were made with the CASA task immoments, integrating over 600 km s^{-1} covering most of the velocity range of the line emission ($>$1.5 × FWHM) This wavelength range is

comparable to previous studies for luminous galaxies (Inoue et al. 2016; Matthee et al. 2017; Hashimoto et al. 2019a). We calculate the signal-to-noise ratios (S/Ns) of the emission lines using 0$.\!\!''$7 diameter circular aperture, by randomly placing apertures on the image and adopting the rms as the noise level. The [O III] and [C II] emission lines are clearly detected in all of our targets at the 4.3–11.8σ significance levels. In addition, the [C II] emission in J1211-0118 and J0217-0208 are spatially well resolved. The [N II] emissions are not detected in our three targets. For all three emission lines for the three targets, total fluxes are measured on the 600 km s^{-1}-integrated maps in 2$''$-radius circular apertures, which can cover the area where spatially extended emission may exist like the [C II]158 μm halos around $z \sim 6$ galaxies reported by Fujimoto et al. (2019). Note that the maximum recoverable scales of our data, 6$''$–7$''$, are larger than the typical size of the [C II] halo, $\sim$2$''$.

In Figure 2, we compare spatial distributions of the [O III] and [C II] with the rest-UV emission including Lyα. We plot the peak pixel positions of the [O III] and [C II] emission with uncertainties with crosses in Figure 2. We estimate the uncertainties of the peak positions using Monte Carlo simulations. In each data set of the target and the emission line, we add artificial sky noises to pixels following a Gaussian random distribution with a standard deviation equal to the 1σ noise of the data, and remeasure the peak positions. We make a series of 1000 simulations for each data set and estimate the uncertainties of the peak positions. We find that the peak
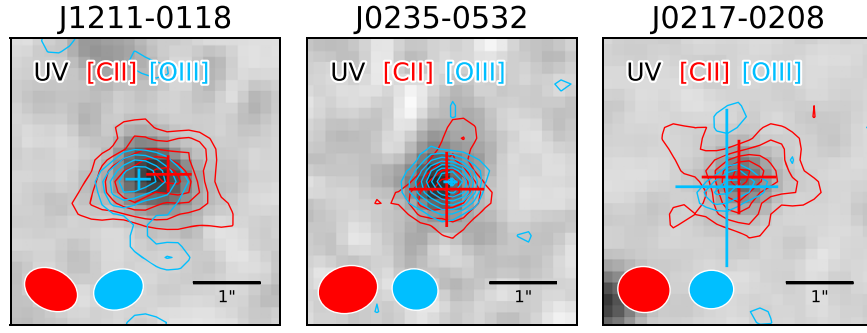
Figure 2. ALMA [C II]158 μm and [O III]88 μm emission maps on rest-UV and Lyα image (the Subaru/HSC z-band). The red and cyan contours show [C II] and [O III] emission, respectively, and are drawn at 1σ intervals from 2σ. The red and cyan crosses show the peak positions, and the sizes show their uncertainties estimated from the Monte Carlo simulations (see text).
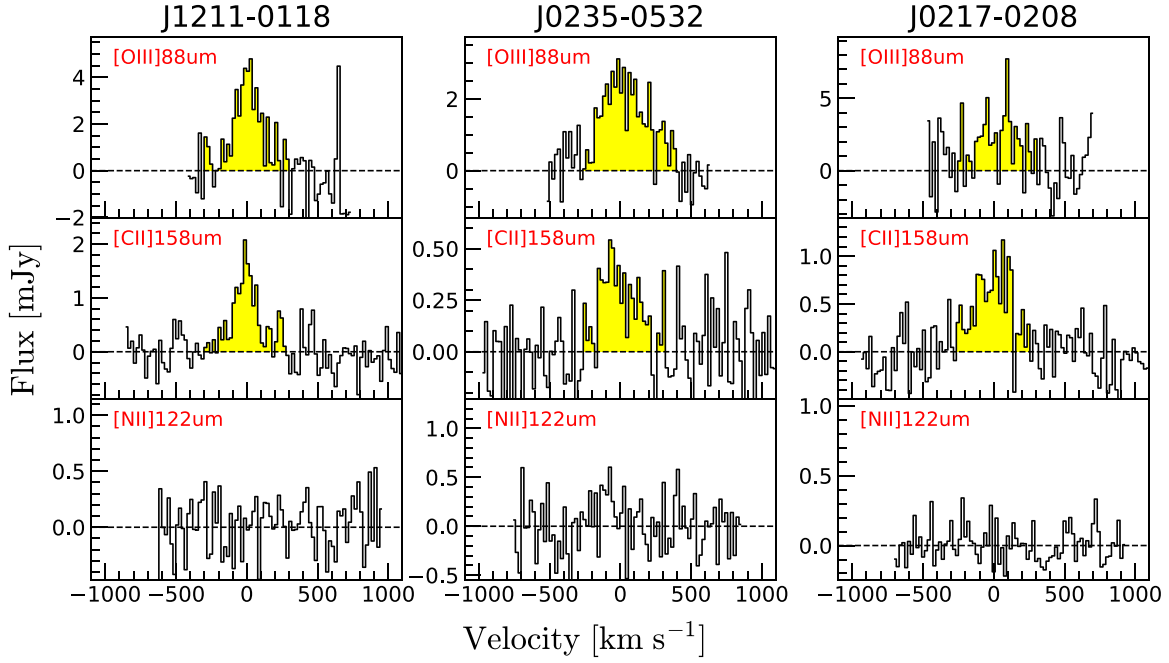

Figure 3. ALMA spectra of our targets after the continuum subtraction. These spectra are extracted from a $0''7$ diameter circular aperture, re-binned to a spectral resolution of 20 km s^{-1}. The velocity zero point is set to the systemic redshift of each target. The [O III] and [C II] emission lines are clearly detected, and their redshifts are consistent within 1σ uncertainties.

positions of [O III] and [C II] agree within 2σ uncertainties in all of our galaxies.

Figure 3 shows spectra around the frequencies of the [O III] 88 μm, [C II]158 μm, and [N II]122 μm lines. We simply fit each spectrum with a single Gaussian profile and the rest-frame [O III]88 μm, [C II]158 μm, or [N II]122 μm frequency (1900.5369, 3393.0062, or 2459.3801 GHz, respectively[17]) that delivers the redshift and full width at half maximum (FWHM). The obtained redshifts and FWHMs are summarized in Table 1. We find that the redshifts based on the [O III] and [C II] lines are consistent within 1σ uncertainties. The FWHMs are 170–390 km s^{-1}. The FWHMs of the [O III] lines seem to be larger than those of the [C II] lines, but they are comparable within 1σ uncertainties (see also Pallottini et al. 2019). We adopt S/N-weighted means of the [O III] and [C II] redshifts as the systemic redshifts of our targets. The systemic redshifts of J1211-0118, J0235-0532, and J0217-0208 are $z_{\rm sys} = 6.0293$, 6.0901, and 6.2037, respectively. The Lyα redshifts measured from the optical spectroscopy are slightly redshifted from the

systemic redshifts, because of the resonant scattering of Lyα. The Lyα velocity offsets are 40–200 km s^{-1}, comparable to previous results (e.g., Hashimoto et al. 2013, 2019a; Erb et al. 2014; Shibuya et al. 2014).

Based on the total fluxes and the systemic redshifts, we calculate luminosities of the emission lines. Table 1 summarized the calculated [O III] and [C II] luminosities of and upper limits for [N II]. Our targets have some of the highest [O III] and [C II] luminosities seen in $z > 6$ LBGs and LAEs.

4.2. $L_{\rm [O\,III]}$–SFR and $L_{\rm [C\,II]}$–SFR Relations

We compare [O III]88 μm and [C II]158 μm luminosities of our targets with previous studies for LBGs and LAEs given SFRs. We usually plot the [C II] (and [O III]) luminosity as a function of SFR because C$^+$ (O^{2+}) ionizing photons are made by massive stars that have recently formed. The left panel of Figure 4 shows the [O III] luminosities as a function of SFR. For our three targets, these SFRs are total SFRs from UV and IR luminosities that are estimated in Section 5.2. We also plot relations for $z \sim 0$ local starburst galaxies (local SBs) and
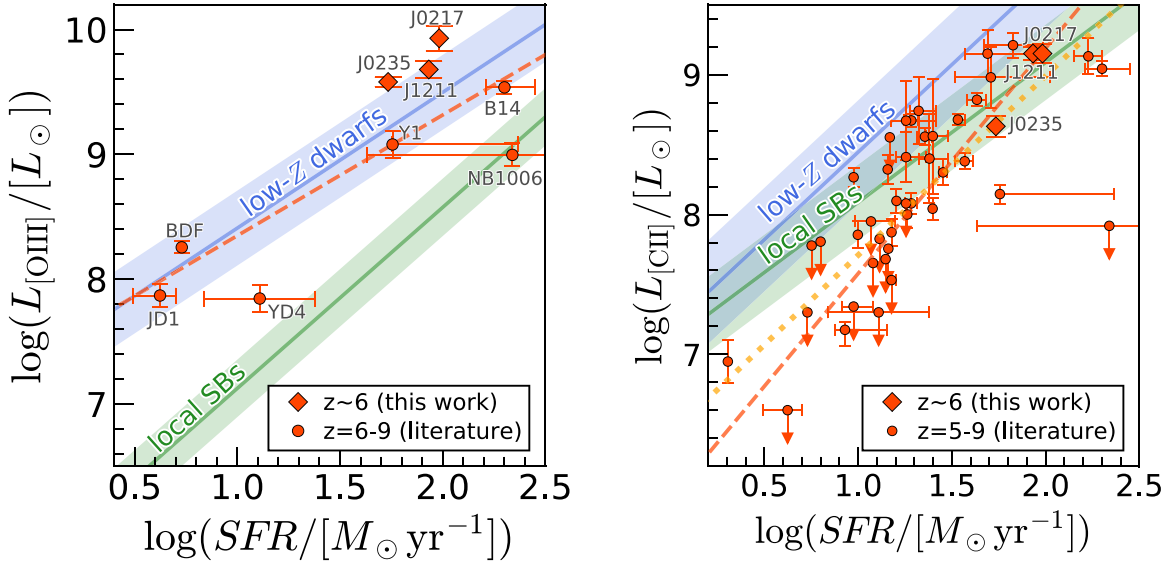
---

[17] http://www.cv.nrao.edu/php/splat/

Figure 4. (Left panel) [O III]88 μm luminosities as a function of the SFR. The red diamonds represent our targets at $z \sim 6$, and the red circles are other $z = 6$–9 LBGs and LAEs in the literature (see Table 2). The red dashed line is the fitting function for the $z = 6$–9 galaxies (see text). The blue and green lines denote relations for $z \sim 0$ low-metallicity dwarf galaxies ("low-Z dwarfs") and starburst galaxies ("local SBs") from de Looze et al. (2014), respectively. The shades correspond to the 1σ dispersion of the relations. (Right panel) Same as the left panel, but for [C II]158 μm luminosities. The red circles are $z = 5$–9 LBGs and LAEs in the literature (see Table 2). The orange dotted line is a fitting function in Schaerer et al. (2020) for ALPINE sample at $z = 4$–6 and $z \sim 6$–9 galaxies (their Figure 6).

low-metallicity dwarf galaxies (low-Z dwarfs) from de Looze et al. (2014), and results of $z = 6$–9 galaxies in the literature (Inoue et al. 2016; Carniani et al. 2017; Laporte et al. 2017a; Hashimoto et al. 2018, 2019a; Tamura et al. 2019), summarized in Table 2. The [O III] luminosities of our targets are comparable to or higher than the relation for the low-metallicity dwarf galaxies of de Looze et al. (2014). Other $z = 6$–9 galaxies are comparable to either of the local relations. The $z = 6$–9 galaxies do not show any deficit relative to the local $L_{\text{[O III]}}$–SFR relations unlike the [C II] case. In the left panel of Figure 4, we plot the following fitting function for the results of $z = 6$–9 galaxies as the red dashed line:

$$\log(L_{\text{[O III]}}/[L_\odot]) = 0.97 \times \log(\text{SFR}/[M_\odot \text{ yr}^{-1}]) + 7.4. \quad (4)$$

The right panel of Figure 4 displays the [C II] luminosities as a function of the SFR. We also plot relations for $z \sim 0$ galaxies and results for $z = 5$–9 galaxies in the literature summarized in Table 2. In contrast to the [O III] luminosities, all of our targets are located below the $L_{\text{[C II]}}$–SFR relation of $z \sim 0$ low-metallicity dwarf galaxies. We find that J1211-0118 and J0217-0208 follow the relation for $z \sim 0$ starburst galaxies, and the [C II] luminosity of J0235-0532 is 0.3 dex lower than that relation. The relatively low [C II] luminosity of J0235-0532 with the strong Lyα emission (EW$^0_{\text{Ly}\alpha} = 41$ Å) is consistent with the anticorrelation between $L_{\text{[CII]}}$/SFR and EW$^0_{\text{Ly}\alpha}$ reported in Harikane et al. (2018b). The red dashed line in the right panel of Figure 4 is the fitting function for the results of $z = 6$–9 galaxies:

$$\log(L_{\text{[C II]}}/[L_\odot]) = 1.6 \times \log(\text{SFR}/[M_\odot \text{ yr}^{-1}]) + 6.0, \quad (5)$$

which is comparable to a fitting function for a combination of the ALMA Large Program to INvestigate C$^+$ at Early Times (ALPINE) data at $z = 4$–6 and $z \sim 6$–9 galaxies in (Schaerer et al. 2020, the orange dotted line in Figure 4 right).

4.3. $L_{\text{[O III]}}/L_{\text{[C II]}}$ Ratios

We plot the [O III]/[C II] luminosity ratio as a function of the SFR and the bolometric luminosities in Figure 5, following previous studies (Hashimoto et al. 2019a, 2019b; Laporte et al. 2019; Bakx et al. 2020). We also plot results of $z = 6$–9 galaxies in the literature and local galaxies studied in the Dwarf Galaxy Survey (Madden et al. 2013; de Looze et al. 2014; Cormier et al. 2015) and the Great Observatories All-sky LIRG Survey (GOALS; Howell et al. 2010; Díaz-Santos et al. 2017). We find that our targets and other $z = 6$–9 galaxies show systematically higher [O III]/[C II] ratios compared to local galaxies, which is consistent with previous results (Inoue et al. 2016; Laporte et al. 2019). In Figure 5, we plot the following fitting functions for the results of $z = 6$–9 galaxies as the red dashed lines:

$$\log(L_{\text{[O III]}}/L_{\text{[C II]}}) = -0.20 \times \log(\text{SFR}/[M_\odot \text{ yr}^{-1}]) + 1.3, \quad (6)$$

$$\log(L_{\text{[O III]}}/L_{\text{[C II]}}) = -0.59 \times \log(L_{\text{bol}}/[L_\odot]) + 7.7. \quad (7)$$

We will discuss the origin of the high [O III]/[C II] ratios in Section 6.1.

4.4. Velocity Fields

We investigate kinematic properties of our targets using [C II] emission, which are detected with high signal to noise ratios and are spatially well resolved in J1211-0118 and J0217-0208. With the CASA task `immoments`, we create flux-weighted velocity (i.e., moment 1) maps and velocity dispersion (i.e., moment 2) maps of [C II] emission of our targets. We only use pixels with $>2\sigma$ detections. Figure 6 shows the velocity and dispersion maps. The [C II] velocity map of J1211-0118 clearly shows a $\sim$220 km s^{-1} velocity gradient. We also identify a gradient of $\sim$250 km s^{-1} in J0217-0208. The velocity dispersions ($\sigma_{\text{tot}} \simeq$ FWHM/2.35) are $\sim$70,

Table 2
Summary of High-redshift Galaxies with ALMA Observations

Name (1)	$z_{\rm spec}$ (2)	$L_{\rm [C\,II]}$ (3)	$L_{\rm [O\,III]}$ (4)	$\rm SFR_{tot}$ (5)	$\rm EW^0_{Ly\alpha}$ (6)	Reference (7)
			LBGs & LAEs			
MACS1149-JD1	9.110	$<4.0 \times 10^6$	$(7.4 \pm 1.6) \times 10^7$	$4.2^{+0.8}_{-1.1}$	10	H18a, L19
A2744-YD4	8.382	$<2.0 \times 10^7$	$(7.0 \pm 1.7) \times 10^7$	$12.9^{+11.1}_{-6.0}$	10.7 ± 2.7	L17a,19
MACS0416-Y1	8.312	$(1.4 \pm 0.2) \times 10^8$	$(1.2 \pm 0.3) \times 10^9$	$57.0^{+175.0}_{-0.2}$	<16.7	Tam19, B20
SXDF-NB1006-2	7.215	$<8.4 \times 10^7$	$(9.9 \pm 2.1) \times 10^8$	219^{+105}_{-176}	>15.4	I16
B14-65666	7.168	$(1.1 \pm 0.1) \times 10^9$	$(3.4 \pm 0.4) \times 10^9$	200^{+82}_{-38}	$3.7^{+1.7}_{-1.1}$	H19, F16
BDF-3299	7.109	$(4.9 \pm 0.6) \times 10^7$	$(1.8 \pm 0.2) \times 10^8$	5.4	38.8	C17, M15
J0217-0208	6.204	$(1.4 \pm 0.2) \times 10^9$	$(8.5 \pm 2.0) \times 10^9$	96	15 ± 1	This work
J0235-0532	6.090	$(4.3 \pm 0.7) \times 10^8$	$(3.8 \pm 0.3) \times 10^9$	54	41 ± 2	This work
J1211-0118	6.029	$(1.4 \pm 0.1) \times 10^9$	$(4.8 \pm 0.7) \times 10^9$	86	6.9 ± 0.8	This work
z8-GND-5296	7.508	$<3.5 \times 10^8$	...	14.7	8	S15, F12
A1689-zD1	7.5	$<8.9 \times 10^7$	...	$11.7^{+4.1}_{-2.2}$	<27	W15
COSMOS13679	7.154	$(7.4 \pm 1.7) \times 10^7$	...	15.1	15	P16
BDF-521	7.109	$<6.0 \times 10^7$	...	5.6	64	M15, V11
IOK-1	6.965	$<3.4 \times 10^7$	...	15.1 ± 0.9	43	O14, O12
COS-3018555981	6.854	$(4.7 \pm 0.5) \times 10^8$	...	19.2 ± 1.6	<2.9	S18, L17
SDF46975	6.844	$<5.8 \times 10^7$	...	14.5	43	M15, O12
COS-2987030247	6.816	$(3.6 \pm 0.5) \times 10^8$	...	22.7 ± 2.0	$16.2^{+5.2}_{-5.5}$	S18, L17
RXJ1347-1145	6.765	$(1.5^{+0.2}_{-0.4}) \times 10^7$	...	$8.5^{+5.9}_{-1.0}$	26 ± 4	B16
NTTDF6345	6.701	$(1.9 \pm 0.3) \times 10^8$	...	9.4	15	P16
UDS16291	6.638	$(7.2 \pm 1.7) \times 10^7$	...	10.0	6	P16
COSMOS24108	6.629	$(1.0 \pm 0.2) \times 10^8$	...	18.3	27	P16
CR7	6.604	$(2.0 \pm 0.4) \times 10^8$	...	28.4 ± 1.3	211 ± 20	M17, So15
Himiko	6.595	$(1.2 \pm 0.2) \times 10^8$	...	19.2 ± 1.3	78^{+8}_{-6}	C18, O13
UDS4821	6.561	$<6.8 \times 10^7$	...	13	48	C17
HCM6A	6.56	$<6.5 \times 10^7$	...	6.3	25.1	K13, H02
MASOSA	6.543	$<6.6 \times 10^7$	...	$9.5^{+2.5}_{-1.3}$	145^{+50}_{-43}	M19
VR7	6.529	$(4.8 \pm 0.4) \times 10^8$	...	$34.0^{+3.2}_{-1.3}$	34^{+4}_{-4}	M19
COSMOS20521	6.36	$<4.8 \times 10^7$	...	14	10	C17
GOODS3203	6.27	$<1.2 \times 10^8$	...	18	5	C17
CLM1	6.176	$(2.4 \pm 0.3) \times 10^8$	...	37 ± 4	50	W15, C03
BDF2203	6.12	$(1.3 \pm 0.3) \times 10^8$	...	16	3	C17
WMH5	6.076	$(6.6 \pm 0.8) \times 10^8$	...	43 ± 5	13 ± 4	W15, W13
NTTDF2313	6.07	$<4.5 \times 10^7$	...	12	0	C17
A383-5.1	6.029	$(8.9 \pm 3.1) \times 10^6$	...	2.0	138	K16, St15
WMH13	5.985	$(1.1 \pm 0.2) \times 10^8$	...	24.9	27	F19
HZ1	5.690	$(2.5 \pm 1.9) \times 10^8$	...	24^{+6}_{-3}	$5.3^{+2.6}_{-4.1}$	C15, M12
NB816-S-61269	5.684	$(2.1 \pm 0.5) \times 10^8$	...	14.4	93.3	F19
HZ2	5.670	$(3.6 \pm 3.4) \times 10^8$	...	25^{+5}_{-2}	6.9 ± 2.0	C15
HZ10	5.659	$(1.3 \pm 0.4) \times 10^9$	...	169^{+32}_{-27}	$24.5^{+9.2}_{-11.0}$	C15, M12
HZ9	5.548	$(1.6 \pm 0.3) \times 10^9$	...	67^{+30}_{-20}	$14.4^{+6.8}_{-5.4}$	C15, M12
HZ3	5.546	$(4.7 \pm 3.0) \times 10^8$	...	18^{+8}_{-3}	<3.6	C15
HZ4	5.540	$(9.5 \pm 4.8) \times 10^8$	...	51^{+54}_{-18}	$10.2^{+0.9}_{-4.4}$	C15, M12
HZ6	5.290	$(1.4 \pm 0.6) \times 10^9$	...	49^{+44}_{-12}	$8.0^{+12.1}_{-7.3}$	C15, M12
HZ7	5.250	$(5.5 \pm 3.0) \times 10^8$	...	21^{+5}_{-2}	9.8 ± 5.5	C15
HZ8	5.148	$(2.6 \pm 1.1) \times 10^8$	...	18^{+5}_{-2}	$27.1^{+12.9}_{-14.7}$	C15, M12
			SMGs			
SPT0311-58-E	6.900	$(5.4 \pm 0.5) \times 10^9$	$(6.9 \pm 0.7) \times 10^9$	540 ± 175	...	M18
SPT0311-58-W	6.900	$(1.0 \pm 0.2) \times 10^{10}$	$(5.7 \pm 1.1) \times 10^9$	2900 ± 1800	...	M18
J2100-SB	6.0806	$(1.8 \pm 0.9) \times 10^9$	$(2.9 \pm 0.1) \times 10^9$	284 ± 30	...	W18
COSMOS-AzTEC-1	4.342	$(6.3 \pm 0.6) \times 10^9$	$(2.2 \pm 0.7) \times 10^9$	1169^{+11}_{-274}	...	Tad18,19

Note. (1) Object name. (2) Redshift determined with Lyα, Lyman break, rest-frame UV absorption lines, [C II]158 μm, or [O III]88 μm. (3) [C II]158 μm luminosity or its 3σ upper limit in units of $L_\odot$. (4) [O III]88 μm luminosity in units of $L_\odot$. (5) Total SFR (=$\rm SFR_{UV}$ + $\rm SFR_{IR}$) in units of $M_\odot$ yr^{-1}. (6) Rest-frame Lyα EW not corrected for the inter-galactic medium (IGM) absorption in units of Å. (7) Reference (B17: Bradač et al. 2017, B20: Bakx et al. 2020, C03: Cuby et al. 2003, C15: Capak et al. 2015, C17: Carniani et al. 2017, C18a: Carniani et al. 2018b, C18b: Carniani et al. 2018a, F13: Finkelstein et al. 2013, F16: Furusawa et al. 2016, F19: Fujimoto et al. 2019, H02: Hu et al. 2002, H18a: Hashimoto et al. 2018 H19: Hashimoto et al. 2019a I16: Inoue et al. 2016, K13: Kanekar et al. 2013, K16: Knudsen et al. 2016, L17a: Laporte et al. 2017a, L17b: Laporte et al. 2017b, L19: Laporte et al. 2019 M12: Mallery et al. 2012, M15: Maiolino et al. 2015, M17: Matthee et al. 2017, M18: Marrone et al. 2018, M19: Matthee et al. 2019, O12: Ono et al. 2012, O13: Ouchi et al. 2013, O14: Ota et al. 2014, P16: Pentericci et al. 2016, S12: Shibuya et al. 2012, Sc15: Schaerer et al. 2015, So15: Sobral et al. 2015, St15: Stark et al. 2015a, S18: Smit et al. 2018, Tad18: Tadaki et al. 2018, Tad19: Tadaki et al. 2019, Tam19: Tamura et al. 2019, V11: Vanzella et al. 2011, W13: Willott et al. 2013, Wa15: Watson et al. 2015, Wi15: Willott et al. 2015, W18: Walter et al. 2018).
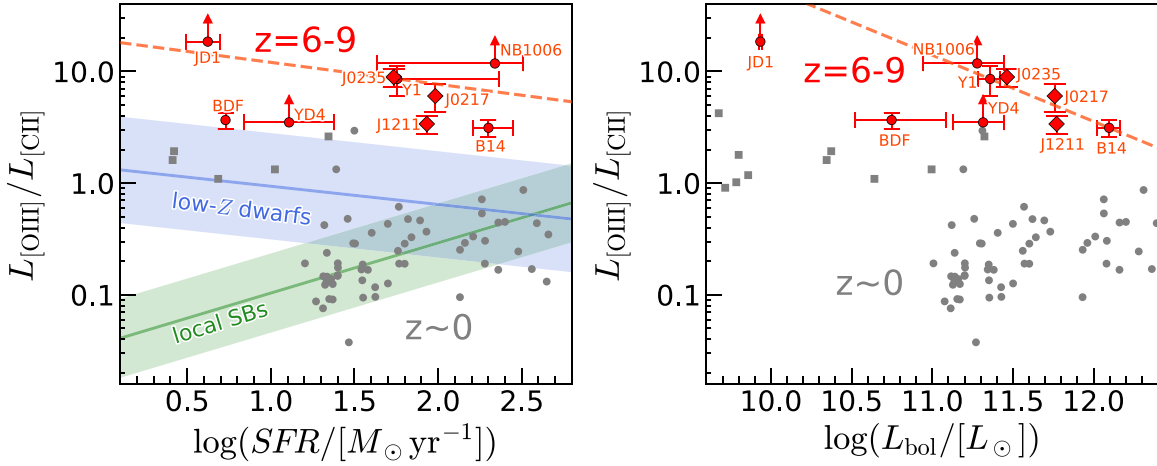
Figure 5. (Left panel) [O III]/[C II] ratios as a function of the SFR. The red diamonds represent our targets at $z \sim 6$, and the red circles are other $z = 6$–9 LBGs and LAEs in the literature (see Table 2). The red dashed line is the fitting function for the $z = 6$–9 galaxies (see text). The gray diamonds and circles denote $z \sim 0$ galaxies from the Dwarf Galaxy Survey (Madden et al. 2013; de Looze et al. 2014; Cormier et al. 2015) and GOALS (Howell et al. 2010; Díaz-Santos et al. 2017), respectively. The blue and green lines denote relations for $z \sim 0$ low-metallicity dwarf galaxies ("low-Z dwarfs") and starburst galaxies ("local SBs") from de Looze et al. (2014), respectively. The shades correspond to the 1σ dispersion of the relations. We find that the [O III]/[C II] ratios of the $z = 6$–9 galaxies are systematically higher than those of $z \sim 0$ galaxies. (Right panel) Same as the left panel, but as a function of the bolometric luminosity, $L_{\rm bol}$. The bolometric luminosity is estimated as a summation of the UV and IR luminosities. The UV and IR luminosities of galaxies in the literatures are taken from Hashimoto et al. (2019a).
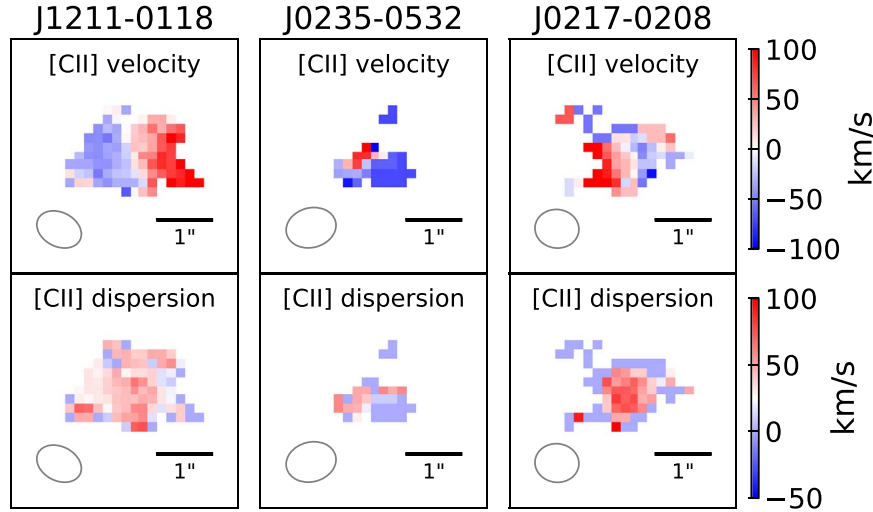
Figure 6. Mean velocity map (upper panel) and velocity dispersion (lower panel) of [C II] in our targets. We can identify velocity gradients in J1211-0118 and J0217-0208, suggesting that they are consistent with rotation-dominated systems.

$\sim$110, and $\sim$130 km s^{-1} for J1211-0118, J0235-0532, and J0217-0208, respectively. Given the low angular resolution of the observations, there are various interpretations of the velocity gradients. A rotating galaxy disk would be one interpretation.

We apply an observational criterion for the classification of rotation- and dispersion-dominated systems, $\Delta v_{\rm obs}/2\sigma_{\rm tot} = 0.4$, where $\Delta v_{\rm obs}$ and $\sigma_{\rm tot}$ are the full observed velocity gradient and the velocity dispersions (Förster Schreiber et al. 2009). We find that $\Delta v_{\rm obs}/2\sigma_{\rm tot} = 1.6$ and 0.96 for J1211-0118 and J0217-0208, respectively, indicating that these two galaxies are consistent with rotation-dominated systems. These values ($\Delta v_{\rm obs}/2\sigma_{\rm tot} > 0.4$) are contrast to those of other systems that are interpreted as galaxy mergers (e.g., Bañados et al. 2019).

5. Dust Continua

5.1. Detections and Upper Limits

Figure 7 shows the continuum emission maps of our targets. We calculate the S/Ns of the dust continuum using 0″7 diameter circular aperture, by randomly placing apertures on the image and adopting the rms as the noise level. We detect dust-continuum emission at $\sim$120 μm from J1211-0118 and J0217-0208 at 5.3σ and 7.1σ significance levels, respectively. We also identify dust continua of J1211-0118 and J0217-0208 at $\sim$160 μm, which are useful to constrain dust temperatures of these galaxies (see Section 5.2). We do not detect dust-continuum emission from J0235-0532. We compare spatial positions and morphologies of these dust-continuum emissions with the rest-UV emission in Figure 8. In J1211-0118 and J0217-0208, the peak positions of the dust emission

J1211-0118   J0235-0532   J0217-0208
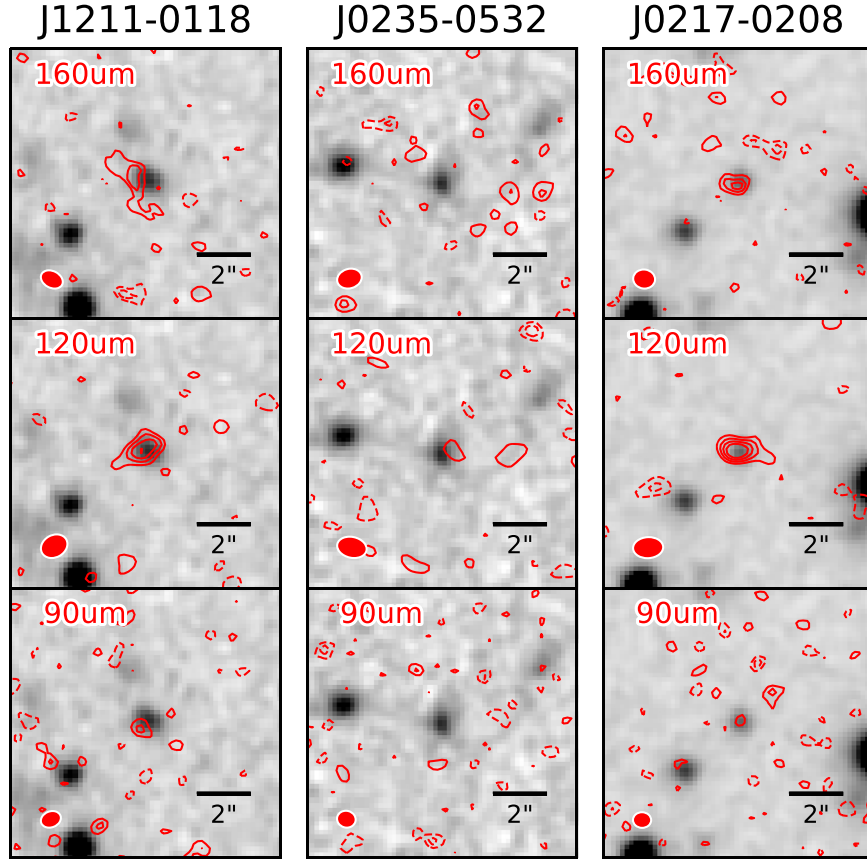
Figure 7. Dust continuum emission of our targets. The red contours are dust emission at $\lambda_{\rm rest} = 160\,\mu$m, 120 μm, and 90 μm, and are drawn at 1σ intervals from $\pm 2\sigma$ to $\pm 5\sigma$. Positive and negative contours are shown by the solid and dashed lines, respectively. The backgrounds are rest-UV and Lyα image (the Subaru/HSC z-band). The images are $10'' \times 10''$, and the red ellipses at the lower left corner indicate the synthesized beam sizes of ALMA.

J1211-0118   J0235-0532   J0217-0208
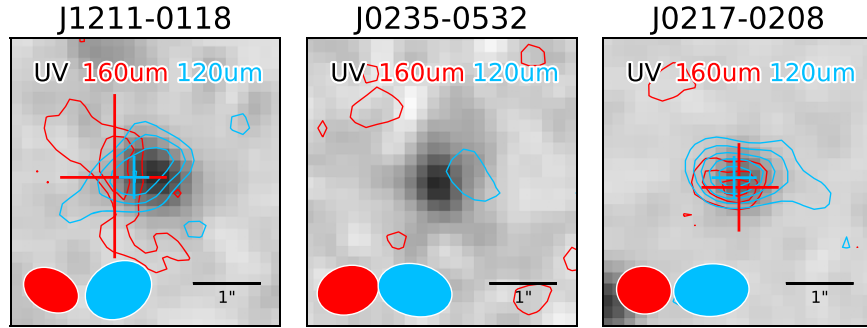
Figure 8. ALMA dust emission maps on rest-UV and Lyα image (the Subaru/HSC z-band). The red and cyan contours show dust emission at $\lambda_{\rm rest} = 160\,\mu$m and 120 μm, respectively, and are drawn at 1σ intervals from 2σ. The red and cyan crosses show the peak positions, and the size show their uncertainties estimated from the Monte Carlo simulations.

overlap with the rest-UV counterparts, given the uncertainties of the peak determination.

5.2. $L_{\rm IR}$ and $T_{\rm dust}$ Estimates

We estimate IR luminosities, $L_{\rm IR}$, by integrating the modified blackbody radiation over 8–1000 μm. We fit the observed fluxes with the modified blackbody by varying the IR luminosity and dust temperatures, $T_{\rm dust}$. We fix the dust emissivity to $\beta_{\rm d} = 1.5$, but the effect of this assumption is not significant for our conclusions. For example, if we change the dust emissivity in $1 < \beta_{\rm d} < 3$, the IR luminosity varies only <0.1 dex. The CMB heating and attenuation effects are included following formulas by Da Cunha et al. (2013). In the fitting, we require that the dust

temperature must be higher than the CMB temperature at the redshift of the galaxy (~ 20 K at $z \sim 6$).

Figure 9 shows the dust spectral energy distributions (SEDs) and the best-fit models for our targets. We obtain IR luminosities and dust temperatures of $(L_{\rm IR}, T_{\rm dust}) = (3.2^{+18.7}_{-1.7} \times 10^{11}\,L_\odot, 38^{+34}_{-12}$ K) and $(1.4^{+2.5}_{-0.3} \times 10^{11}\,L_\odot, 25^{+19}_{-5}$ K), for J1211-0118 and J0217-0208, respectively. These IR luminosities ($L_{\rm IR} > 10^{11}\,L_\odot$) correspond to luminous infrared galaxies (LIRGs) in the local universe. These dust temperatures are comparable to other $z > 6$ galaxies (Knudsen et al. 2017; Hashimoto et al. 2019a) and theoretical simulations (Behrens et al. 2018). Although the IR luminosity is degenerate with the dust temperature, shown in the error contours in Figure 9, the IR
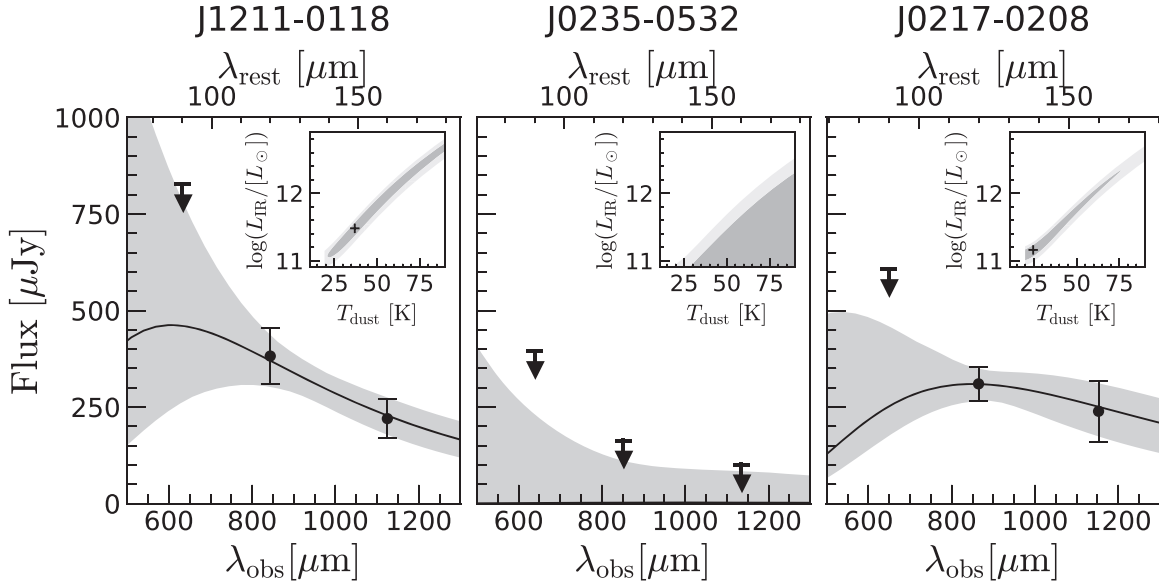
Figure 9. Dust SEDs of our targets. The black circles and downward arrows are our observations. The black solid curves and the shade regions show the best-fit modified blackbody models and the 1σ uncertainties. The inset panels show error contours indicating the 68% and 95% confidence regions. The black crosses denote the best-fit parameters.

luminosities range in $1.1 \times 10^{11} < L_{\rm IR}/L_\odot < 7.9 \times 10^{12}$ and $1.0 \times 10^{11} < L_{\rm IR}/L_\odot < 2.2 \times 10^{12}$ for J1211-0118 and J0217-0208, respectively, within the 1σ confidence regions in the error contours. For J0235-0532, we obtain the 3σ upper limit of $L_{\rm IR} \times T_{\rm dust} < 1.3 \times 10^{13} L_\odot$ K. Since we want to compare our observations with previous studies including Hashimoto et al. (2019a), who assume $T_{\rm dust} = 50$ K for galaxies without continuum detections, we adopt $L_{\rm IR} < 2.5 \times 10^{11} L_\odot$ assuming $T_{\rm dust} = 50$ K as the fiducial value for J0235-0532.

5.3. IRX–$\beta_{\rm UV}$ Relation

We investigate whether our targets follow the known IRX–β relations, or show IRX values below the relations. We estimate the UV slope β using the Subaru/HSC photometry and spectroscopic properties of the Lyα emission lines. Based on the HSC z- and y-band magnitudes, redshifts, and Lyα EWs, we estimate the UV spectral slope to be $\beta_{\rm UV} = -2.0 \pm 0.5$, -2.6 ± 0.6, and -0.1 ± 0.5 for J1211-0118, J0235-0532, and J0217-0208, respectively. Note that the HSC z and y bands correspond to the rest-frame wavelength of 1300–1500 Å.

Figure 10 shows the IRX values of our targets as a function of the UV slope $\beta_{\rm UV}$. We find that J1211-0118 follows the Calzetti IRX–$\beta_{\rm UV}$ relation, similar to A1689-zD1 (Watson et al. 2015), A2744-YD4 (Laporte et al. 2017a, 2019), and B14-65666 (Hashimoto et al. 2019a). The upper limit of J0235-0532 is consistent with both the Calzetti, Takeuchi, and SMC relations. The IRX value of J0217-0208 is lower than the SMC relation, even if the IR luminosity is $L_{\rm IR} = 2.2 \times 10^{12} L_\odot$ (the dashed error bar). Note that the wavelength ranges used to derive $\beta_{\rm UV}$ differ from our sample and the others compared here (see also Hashimoto et al. 2019a); NIR imaging data are necessary to estimate $\beta_{\rm UV}$ in the same wavelength ranges as the other studies.

There are several possibilities for the physical origins of the low IRX value of J0217-0208. One is the geometry effect (e.g., Faisst et al. 2017). Depending on the geometry and the viewing
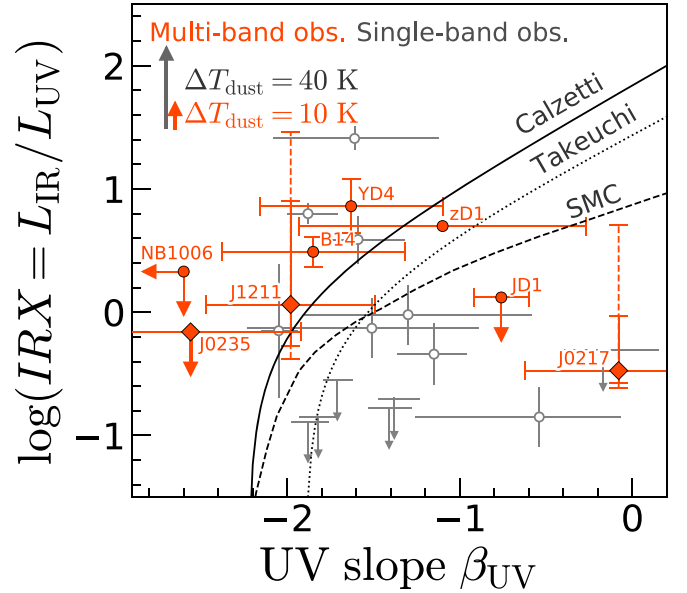
Figure 10. IRX as a function of the UV slope $\beta_{\rm UV}$. The red diamonds represent our targets at $z \sim 6$, and the red circles show the IRX values of $z > 7$ galaxies with multi-band observations taken from Hashimoto et al. (2019a). The dashed error bars show the range of IRX within the 1σ confidence regions in the error contours in Figure 9. The gray circles and upper limits denote other $z > 5$ galaxies without temperature determinations (Barisic et al. 2017). The solid, dotted, and dashed curves show the Calzetti extinction curve (Meurer et al. 1999; Calzetti et al. 2000), the modified curve by Takeuchi et al. (2012), and the SMC extinction curve (Pettini et al. 1998), respectively. The black and red upward arrows show offsets of IRX with higher dust temperatures by 40 K and 10 K, respectively.

angle of the observer, the dust clouds might be spatially offset from the line of sight and the UV light can escape from the galaxy without being attenuated, which would cause the low IRX value. AGN activity also can explain the offset in the IRX–$\beta_{\rm UV}$ plot. Saturni et al. (2018) show that quasars have lower IRX values given the UV slope, similar to $z \sim 5-6$
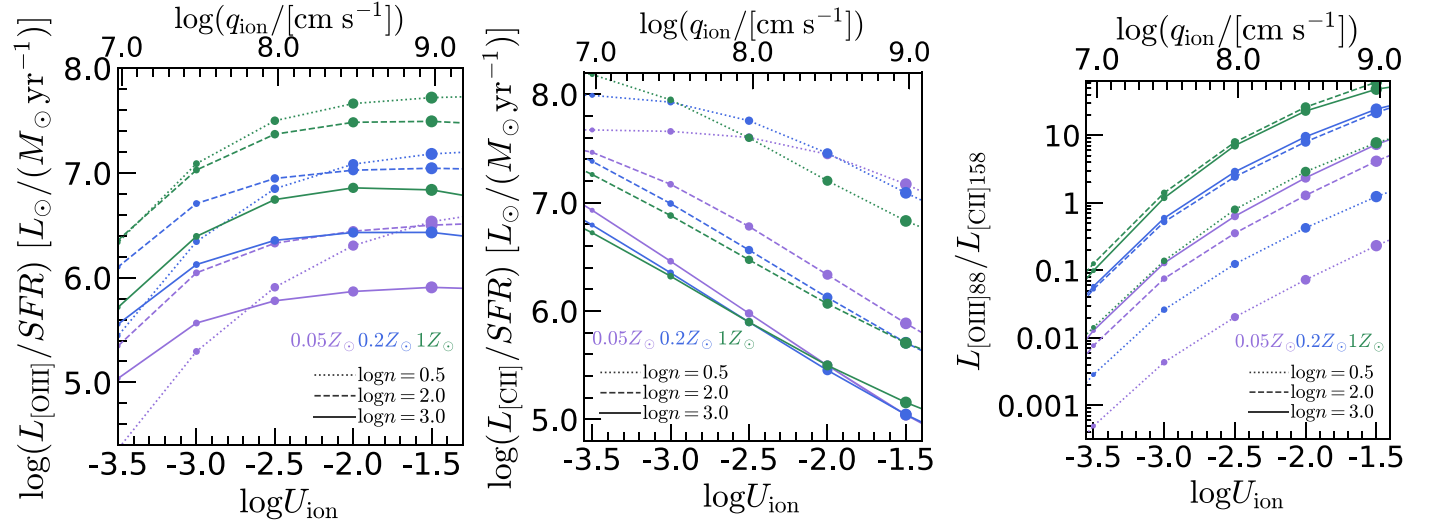
Figure 11. Cloudy calculation results for $L_{\text{[O III]}}/SFR$ (left panel), $L_{\text{[C II]}}/SFR$ (middle panel), and $L_{\text{[O III]}}/L_{\text{[C II]}}$ (right panel) ratios as functions of the ionization parameter. The purple, blue, and green lines are results for metallicities of $Z = 0.05\,Z_\odot$, $0.2\,Z_\odot$, and $1.0\,Z_\odot$, respectively. The dotted, dashed, and solid lines correspond to densities of $\log(n_H/[\text{cm}^{-3}]) = 0.5$, 2.0, and 3.0, respectively. The larger circles indicate higher ionization parameters, from $\log U_{\text{ion}} = -4.0$ to -0.5 with a step size of 0.5.

galaxies in Capak et al. (2015), because UV slopes of AGNs are redder than those of galaxies in $M_{\text{UV}} \gtrsim -24$ mag. Ferrara et al. (2017) suggest that the high fraction of dust locked inside the molecular gas without internal illumination can explain the low IRX value.

5.4. Dust Mass

Based on the observed fluxes at $\sim 160\,\mu$m and the estimated temperatures, we estimate the dust masses in our targets. Assuming a dust mass absorption coefficient $\kappa = \kappa_0(\nu/\nu_0)^{\beta_d}$, where $\kappa_0 = 10$ cm^2 g^{-1} at $250\,\mu$m (Hildebrand 1983), we estimate the dust masses to be $M_{\text{dust}} = 3.0^{+10.5}_{-2.3} \times 10^7\,M_\odot$, $< 6.9 \times 10^6\,M_\odot$ (3σ), and $1.9^{+73.5}_{-1.6} \times 10^8\,M_\odot$ for J1211-0118, J0235-0532, and J0217-0208, respectively. Using an empirical relation between the UV magnitude and stellar mass for $z \sim 6$ LBGs (Song et al. 2016), the stellar masses of our targets are estimated to be $\sim 3 \times 10^{10}\,M_\odot$. The inferred dust-to-stellar mass ratios are $\log(M_{\text{dust}}/M_*) \sim -3.0$, < -3.6, and -2.2 for J1211-0118, J0235-0532, and J0217-0208, respectively. These dust-to-stellar mass ratios are relatively lower than the value for B14-65666 at $z = 7$ ($\log(M_{\text{dust}}/M_*) \sim -1.9$; Hashimoto et al. 2019a), but within the range observed in $z \sim 0$ galaxies (Rémy-Ruyer et al. 2015). These ratios can be reproduced by the supernova (SN) and AGB star model with grain growth in Mancini et al. (2015). Note that our ALMA data probes 90, 120, and $160\,\mu$m in the rest frame. Since the longest wavelength corresponds to ~ 20 K in the Wien law, comparable to the CMB temperature, no cooler dust exists unless the CMB radiation was shielded. On the other hand, dust emission with the CMB temperature (~ 20 K at $z \sim 6$) cannot be detected with interferometers like ALMA (Da Cunha et al. 2013). In the case that there is dust whose temperature is ~ 20 K in the targeted galaxies, such dust would be missed in observations presented here, causing a large uncertainty in dust mass estimates.

6. Discussion

6.1. Origin of High $L_{\text{[O III]}}/L_{\text{[C II]}}$ Ratios at $z = 6$–9

In Section 4.3, we find that the [O III]/[C II] ratios of the $z = 6$–9 galaxies are systematically higher than those of $z \sim 0$ galaxies. In order to discuss the origin of the high [O III]/[C II] ratios of the $z = 6$–9 galaxies, we conduct model calculations including both H II regions and photodissociation regions (PDRs) using Cloudy (Ferland et al. 1998, 2017) version 17.01, following Nagao et al. (2011, 2012). We include PDRs because [C II] emission mainly comes from PDRs (Cormier et al. 2019). We assume a pressure-equilibrium gas cloud with a plain-parallel geometry that is characterized by certain hydrogen gas densities at the ionization front (n_H), metallicity (Z), and ionization parameters U_{ion}. Here we examine gas clouds with $\log(n_H/[\text{cm}^{-3}]) = 0.5$, 2.0, and 3.0, and $Z = 0.05$, 0.2, and $1.0\,Z_\odot$ for $-4.0 \leqslant \log U_{\text{ion}} \leqslant -0.5$ with a step of 0.5. Note that with the very high U_{ion} value such as $\log U_{\text{ion}} = -0.5$, the high pressure would squash the ionized gas (Yeh & Matzner 2012). The input continuum is a spectrum of a burst star formation model with an age of 1 Myr and Salpeter (1955) IMF with lower and upper mass cutoffs of $1\,M_\odot$ and $100\,M_\odot$ for binary populations, calculated with the BPASS v2.1 model (Eldridge et al. 2017). The stellar metallicity is equal to the gas metallicity. The relative chemical composition of the gas cloud is scaled to the solar elemental abundance ratios except for helium, which follows an equation in Groves et al. (2004). The nitrogen abundance is also scaled to the solar abundance, although it is possible that the nitrogen abundance ratio changes due to its secondary element nature. Orion-type graphite and silicate grains are included. Calculations are stopped at the depth of $A_V = 100$ mag to cover the whole [C II] emitting regions, following Abel et al. (2005).

In the left panel of Figure 11, we plot $L_{\text{[O III]}}/SFR$ ratios as a function of the ionization parameter. The SFRs of the models are derived from Hα luminosities using Equation (2) of Kennicutt (1998), and are converted to values in the Chabrier (2003) IMF by multiplying by 0.63. The uncertainty of the
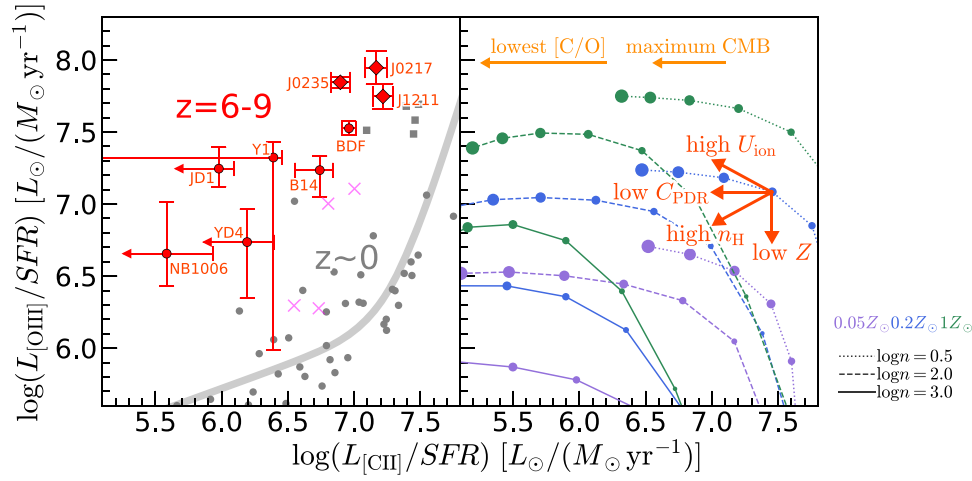
Figure 12. (Left panel) $L_{\rm [O\,III]}$/SFR and $L_{\rm [C\,II]}$/SFR ratios. The red diamonds represent our targets at $z \sim 6$, and the red circles are other $z = 6$–9 LBGs and LAEs in the literature (see Table 2). The gray squares and circles denote $z \sim 0$ galaxies from the Dwarf Galaxy Survey (Madden et al. 2013; de Looze et al. 2014; Cormier et al. 2015) and GOALS (Howell et al. 2010; Díaz-Santos et al. 2017), respectively. The magenta crosses shows SMGs at $z = 4.4$, 6.1, and 6.9 from Tadaki et al. (2018, 2019), Walter et al. (2018), and Marrone et al. (2018), respectively (see Table 2). The $L_{\rm [C\,II]}$/SFR ratios of the $z = 6$–9 galaxies are systematically lower than those of $z \sim 0$ galaxies with similar $L_{\rm [O\,III]}$/SFR ratios. (Right panel) Cloudy calculation results for the $L_{\rm [O\,III]}$/SFR and $L_{\rm [C\,II]}$/SFR ratios. The purple, blue, and green lines are results for metallicities of $Z = 0.05\,Z_\odot$, $0.2\,Z_\odot$, and $1.0\,Z_\odot$, respectively. The dotted, dashed, and solid lines correspond to densities of $\log(n_{\rm H}/[{\rm cm}^{-3}]) = 0.5$, 2.0, and 3.0, respectively. The larger circles indicate higher ionization parameters, from $\log U_{\rm ion} = -4.0$ to -0.5 with a step size of 0.5. The red arrows show directions of the shifts in the $L_{\rm [O\,III]}$/SFR–$L_{\rm [C\,II]}$/SFR plane by higher ionization parameter, lower PDR covering fraction, higher density, and lower metallicity (see text for details). The orange arrows indicate maximum shifts in $L_{\rm [C\,II]}$/SFR by the lower C/O ratio and the CMB attenuation effect.

conversion in Kennicutt (1998) is roughly $\sim$30% (0.1 dex), which does not affect our conclusions. The $L_{\rm [O\,III]}$/SFR ratio increases with increasing ionization parameter, because more ionizing photons are used to produce O^{2+}. Since the critical density of the [O III]88 μm is 510 cm^{-3} for collision with electrons, the ratio decreases with increasing the density from $\log(n_{\rm H}/[{\rm cm}^{-3}]) = 2.0$ to $\log(n_{\rm H}/[{\rm cm}^{-3}]) = 3.0$. Also, the ratio decreases with decreasing metallicity at $0.05 < Z/Z_\odot < 1.0$, because the lower abundance of the oxygen in the H II regions.

The middle panel of Figure 11 shows $L_{\rm [C\,II]}$/SFR ratios as a function of the ionization parameter. The $L_{\rm [C\,II]}$/SFR ratio decreases with increasing ionization parameter, because the volume of PDRs decreases due to the larger H II regions with more ionizing photons, and more C^+ are ionized to C^{2+} (see also Ferrara et al. 2019). We find that higher hydrogen densities also make lower $L_{\rm [C\,II]}$/SFR ratios, because the density in PDRs is higher than that in H II regions in the constant pressure assumption, and it exceeds the critical density of [C II]158 μm for hydrogen, 2800 cm^{-3}. The ratio does not strongly change with metallicity. As discussed in Kaufman et al. (2006), the carbon abundance is proportional to the metallicity, Z, while the PDR column density is proportional to $1/Z$, as long as shielding of FUV photons is dominated by dust (assuming a constant dust-to-metal ratio) and the gas column density is large enough. Since the [C II] emission mainly comes from PDRs, the [C II] luminosity does not strongly depend on the metallicity ($L_{\rm [C\,II]} \propto Z \times 1/Z = {\rm constant}$, see also Pallottini et al. 2019; Ferrara et al. 2019).

We also show calculated [O III]/[C II] ratios as a function of the ionization parameter in the right panel of Figure 11. The ratio increases with increasing ionization parameter or metallicity. The ratio also increases with increasing the density from $\log(n_{\rm H}/[{\rm cm}^{-3}]) = 0.5$ to $\log(n_{\rm H}/[{\rm cm}^{-3}]) = 2.0$.

Since the SFR is an important parameter describing the amount of ionizing photons, we need to compare both the line luminosities and SFRs of the observations with the models.

Thus we compare $L_{\rm [O\,III]}$/SFR and $L_{\rm [C\,II]}$/SFR ratios of the $z = 6$–9 galaxies with $z \sim 0$ galaxies in the left panel of Figure 12. Our targets (J1211-0118, J0235-0532, and J0217-0208), MACS0416-Y1, B14-65666, and BDF-3299 are located in a region of $6.3 < \log(L_{\rm [C\,II]}/{\rm SFR}) < 7.3$ and $7.2 < \log(L_{\rm [O\,III]}/{\rm SFR}) < 8.0$. These galaxies ("[C II] detected galaxies") have $\sim$0.3–1 dex lower $L_{\rm [C\,II]}$/SFR ratios than $z \sim 0$ galaxies with similar $L_{\rm [O\,III]}$/SFR ratios. On the other hand, MACS1149-JD1, A2744-YD4, and SXDF-NB1006-2 are in $\log(L_{\rm [C\,II]}/{\rm SFR}) < 6.3$ and $6.6 < \log(L_{\rm [O\,III]}/{\rm SFR}) < 7.4$. The $L_{\rm [C\,II]}$/SFR ratios of these galaxies ("[C II] undetected galaxies") are >1 dex lower than $z \sim 0$ galaxies with similar $L_{\rm [O\,III]}$/SFR ratios.

We plot results of the model calculations for $L_{\rm [O\,III]}$/SFR and $L_{\rm [C\,II]}$/SFR ratios in the right panel of Figure 12. Based on these calculations, we discuss the following eight possibilities explaining the observational properties (i.e., $L_{\rm [O\,III]}$/SFR, $L_{\rm [C\,II]}$/SFR, and high [O III]/[C II]) of the $z = 6$–9 galaxies compared to the $z \sim 0$ galaxies:

(A) Higher ionization parameter ($U_{\rm ion}$). Several studies suggest higher ionization parameters in higher redshift galaxies, compared to $z \sim 0$ galaxies ($\log U_{\rm ion} \simeq -3.1$, e.g., Nakajima & Ouchi 2014). As shown in Figures 11 and 12, with increasing $U_{\rm ion}$, $L_{\rm [O\,III]}$/SFR increases while $L_{\rm [C\,II]}$/SFR decreases. Thus high ionization parameters can explain the $L_{\rm [O\,III]}$/SFR and $L_{\rm [C\,II]}$/SFR ratios of both [C II] detected and undetected galaxies at $z = 6$–9. For example, as shown in the left panel of Figure 13, 2.0 dex (1.0 dex) higher ionization parameter can reproduce the >1 dex (0.3–1 dex) systematic offsets of $L_{\rm [C\,II]}$/SFR seen in the [C II] undetected (detected) galaxies at $z = 6$–9, compared to the $z \sim 0$ galaxies, if we fix the metallicity and density. Thus high ionization parameters would be an origin of the high [O III]/[C II] ratios of the $z = 6$–9 galaxies. The high ionization parameters in $z = 6$–9 galaxies are possibly made by young (bursty) or low-metallicity stellar populations with more ionizing
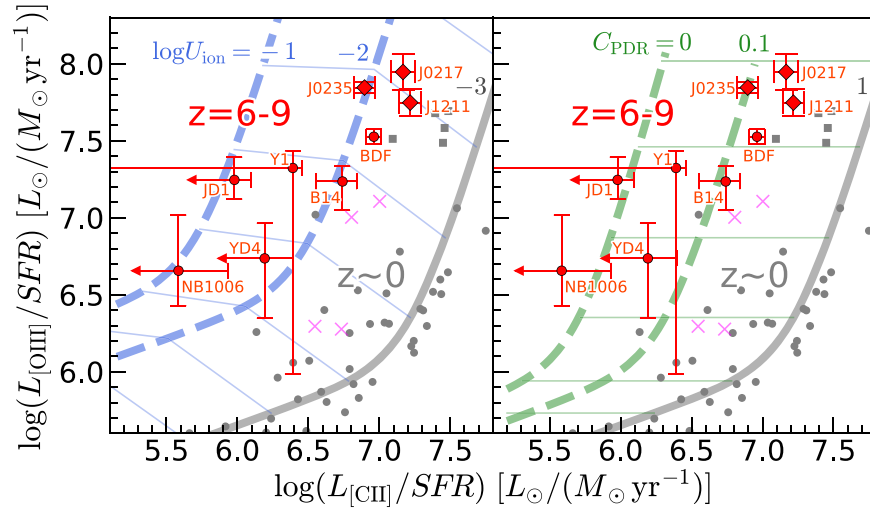
Figure 13. Same as the left panel of Figure 12, but with the model curves with various ionization parameters (left) and PDR covering fractions (right). The solid gray curve shows the ratios for $\log U_{\rm ion} = -3$ and $C_{\rm PDR} = 1$. The dashed blue curves in the left panel are ratios in cases of $\log U_{\rm ion} = -2$ and -1 with $C_{\rm PDR} = 1$. The dashed green curves in the right panel indicate ratios in cases of $C_{\rm PDR} = 0.1$ and 0 with $\log U_{\rm ion} = -3$. The high ionization parameter ($\times 10$–100 higher $U_{\rm ion}$ than $z \sim 0$) or low PDR covering fraction ($C_{\rm PDR} = 0$–0.1) can reproduce the $z = 6$–9 galaxies.

photons, or compact sizes of galaxies with high SFR surface densities (e.g., Shibuya et al. 2015), as predicted by theoretical simulations (e.g., Vallini et al. 2017; Moriwaki et al. 2018). The high SFR surface density could ionize C^+ to C^{2+} and make the H II regions overlapping each other like Figure 15(b), increasing (decreasing) the volume of the H II regions (PDRs). Observations for local starburst galaxies also report a positive correlation between the [O III]/[C II] ratio and the dust temperature (Díaz-Santos et al. 2017; Walter et al. 2018), possibly due to high ionization parameters in high [O III]/[C II] galaxies. Theoretical simulations of Pallottini et al. (2019) and Ferrara et al. (2019) suggest that the burst of star formation enhance the ionization parameter and make the [C II] deficit, although it is not known whether the simulations also quantitatively reproduce the observed high [O III]/[C II] ratios.

(B) Lower gas metallicity (Z). Evolution of the mass–metallicity relation suggests lower metallicities in higher redshift galaxies (e.g., Maiolino et al. 2008). Figures 11 and 12 indicate that with decreasing metallicity, only the $L_{\rm [O III]}/SFR$ ratio decreases, while the $L_{\rm [C II]}/SFR$ ratio does not significantly change. As discussed in the previous paragraph, the [C II] luminosity from the PDR does not strongly depend on the metallicity, as long as shielding of FUV photons is dominated by dust and the gas column density is large enough. Thus changing the metallicity cannot reproduce the systematic offsets seen in $L_{\rm [C II]}/SFR$ of the $z = 6$–9 galaxies.

(C) Higher density ($n_{\rm H}$). Several spectroscopic studies report high electron densities in high-redshift galaxies (e.g., Shimakawa et al. 2015; Sanders et al. 2016; Kashino et al. 2017). As shown in Figures 11 and 12, both $L_{\rm [O III]}/SFR$ and $L_{\rm [C II]}/SFR$ ratios decrease with increasing the hydrogen density due to the collisional de-excitation. Since the $L_{\rm [O III]}/SFR$ ratios of the $z = 6$–9 galaxies are comparable to $z \sim 0$, higher densities cannot reproduce both $L_{\rm [O III]}/SFR$ and $L_{\rm [C II]}/SFR$ of the $z = 6$–9 galaxies simultaneously (Figure 14). More precisely, if we increase the density from $\log(n_{\rm H}/[{\rm cm}^{-3}]) = 0.5$ to 2.0, $L_{\rm [O III]}/SFR$ does not
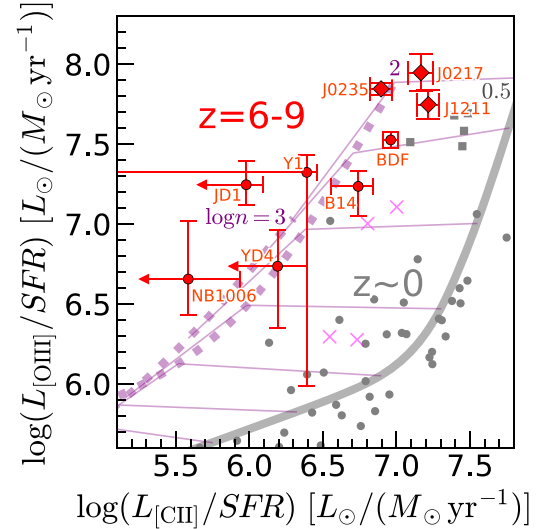
Figure 14. Same as the Figure 13, but with the model curves with various hydrogen densities. The solid gray curve shows the ratios for $\log(n_{\rm H}/[{\rm cm}^{-3}]) = 0.5$. The dotted purple curves are ratios in cases of $\log(n_{\rm H}/[{\rm cm}^{-3}]) = 2.0$ and 3.0 with fixing other parameters. The higher densities ($\log(n_{\rm H}/[{\rm cm}^{-3}]) = 2$–3) cannot explain some of the $z = 6$–9 galaxies (e.g., MACS1149-JD1).

significantly change, while the $L_{\rm [C II]}/SFR$ ratio decreases by ~ 1 dex, because the density in PDRs reaches the critical density of [C II]. Thus as shown in Figure 14, the increase of the density from $\log(n_{\rm H}/[{\rm cm}^{-3}]) = 0.5$ to 2.0 can reproduce a part of the $z = 6$–9 galaxies, but cannot reproduce the < 1 dex lower $L_{\rm [C II]}/SFR$ ratios of some of the $z = 6$–9 galaxies. If we increase the density from $\log(n_{\rm H}/[{\rm cm}^{-3}]) = 2.0$ to 3.0, both the $L_{\rm [C II]}/SFR$ and $L_{\rm [O III]}/SFR$ ratios decreases by ~ 1 dex. As shown in Figure 14, the increase of the density to $\log(n_{\rm H}/[{\rm cm}^{-3}]) = 3.0$ cannot reproduce some of the $L_{\rm [O III]}/SFR$ ratios of the $z = 6$–9 galaxies (e.g., MACS1149-JD1). In order to explain the properties of $z = 6$–9 galaxies with only the increase of the density alone, we need much higher density in PDRs with relatively lower density in H II regions. However,
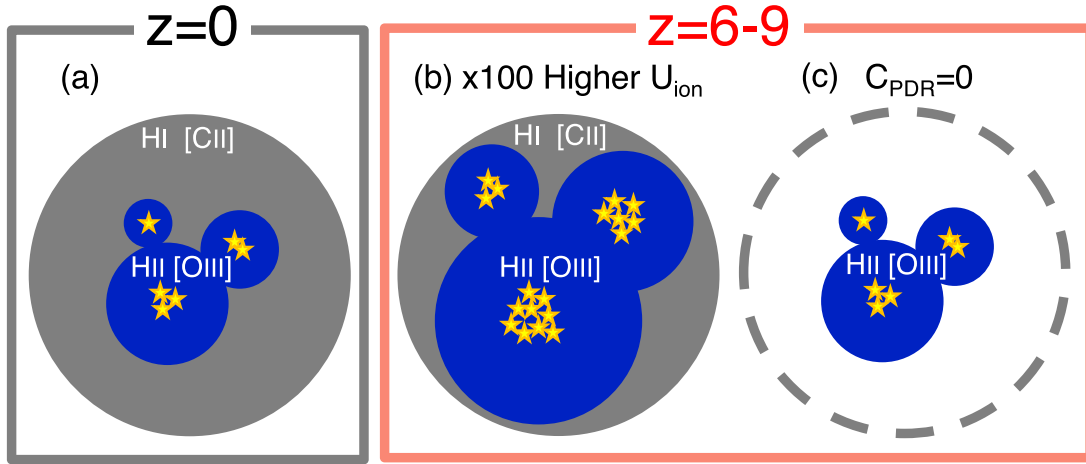
Figure 15. Schematic illustrations of the H II regions and PDRs. The H II regions including the O III emitting gas are presented with blue, and the outer PDRs are shown with gray. Yellow stars are central ionizing sources. (a) A case of an ionization-bounded nebula whose radius is determined by the ionization equilibrium for $z \sim 0$ galaxies. (b) A case of a high-ionization parameter ($U_{\rm ion}$) for $z \sim 6-9$ galaxies. The young stellar population or the compact size would make high $U_{\rm ion}$ and larger H II regions relative to PDRs, resulting in high [O III]/[C II] ratios. (c) A case of a low PDR covering fraction ($C_{\rm PDR}$) for $z \sim 6-9$ galaxies. This illustrates an extreme case of $C_{\rm PDR} = 0$. A low PDR covering fraction makes a low [C II] luminosity. Note that in real galaxies there would be some clumpy molecular gas in the H II regions due to the self shielding like the Orion nebula, leading to next star formation.

theoretical simulations (e.g., Hosokawa & Inutsuka 2005; Wolfire et al. 2010) predict weaker contrast of the density between H II regions and PDRs than the constant pressure assumption used in our calculations (see Figure 2 in Cormier et al. 2019).

(D) Lower C/O ratio. Spectroscopic studies suggest that the C/O abundance ratios of high-redshift galaxies are lower than the solar abundance ratio (e.g., Steidel et al. 2016). Since [C II] and [O III] luminosities depend on the carbon and oxygen abundances, respectively, lower C/O ratios of $z = 6-9$ galaxies may explain the lower $L_{\rm [C\,II]}/{\rm SFR}$ ratio. Steidel et al. (2016) report that C/O abundance ratio of $z \sim 2$ galaxies is $\sim 50\%$ of the solar abundance ratio. Stark et al. (2017) also suggest a $\sim 50\%$ solar abundance ratio for a $z = 7.7$ galaxy. The low C/O ratio would be due to young stellar population in high-redshift galaxies. Oxygen is mainly produced by core-collapse SNe, and therefore has the shortest formation timescales (Maiolino & Mannucci 2019). On the other hand, carbon has contributions from both core-collapse and SNe Ia and from AGB stars, and its average formation timescale is longer than that of oxygen. Thus the low C/O ratio indicates young stellar age with the ongoing production of carbon. The lowest C/O would be C/O $\simeq 0.1({\rm C/O})_\odot$ based on theoretical calculations (e.g., Maiolino & Mannucci 2019) and observations (e.g., Trainor et al. 2016; Cooke et al. 2017). We conduct model calculations again with 50% and 10% solar abundance ratio, [C/O] $= -0.3$ and -1.0, with fixing the oxygen abundance. We find that the $L_{\rm [O\,III]}/{\rm SFR}$ ratio does not change, while the $L_{\rm [C\,II]}/{\rm SFR}$ ratio decreases by 0.3 dex and 0.9 dex, for [C/O] $= -0.3$ and -1.0, respectively. [C/O] $= -0.3$ would explain the 0.3 dex lower $L_{\rm [C\,II]}/{\rm SFR}$ ratio for a part of the [C II] detected galaxies at $z = 6-9$. For the [C II] undetected galaxies, [C/O] $= -1.0$ cannot reproduce the >1 dex lower $L_{\rm [C\,II]}/{\rm SFR}$ ratio. Therefore, low C/O ratios would reproduce a part of the $z = 6-9$ galaxies, but not all of

them. Note that theoretical simulations in Arata et al. (2020) also indicate that low C/O ratios partly contribute to the observed high [O III]/[C II] ratios.

(E) Lower PDR covering fraction ($C_{\rm PDR}$). [O III] emission comes from H II regions, while [C II] emission mainly comes from PDRs (e.g., Kaufman et al. 2006; Cormier et al. 2019). Thus the covering fraction of the PDR (and the neutral H I gas) with respect to the H II region, $C_{\rm PDR}$, is an important parameter to determine the [C II] luminosity and the [O III]/[C II] ratio. Following Cormier et al. (2019), we define the PDR covering fraction, $C_{\rm PDR}$, as a fraction of the number of sightlines with PDRs to that with H II regions,

$$C_{\rm PDR} = \frac{{\rm No.\,of\ sightlines\ with\ PDRs}}{{\rm No.\,of\ sightlines\ with\ H\,II\ regions}}. \quad (8)$$

$C_{\rm PDR}$ is a parameter varying from zero to unity that corresponds to a linear scaling of the PDR intensities. If $C_{\rm PDR} = 1$, all of the H II regions are covered with PDRs (cases (a) and (b) in Figure 15). If $C_{\rm PDR} = 0$, none of the H II regions are covered with PDRs (density-bounded, case (c) in Figure 15). For galaxies with $Z \sim 0.05\,Z_\odot$, the fraction of [C II] emission that comes from H II regions is $\sim 1\%$ (Cormier et al. 2019). As shown in the right panel of Figure 13, if we consider an extreme case of $C_{\rm PDR} = 0$, the [C II] luminosity decreases by $\sim 99\%$ (-2 dex), which can explain the systemically lower $L_{\rm [C\,II]}/{\rm SFR}$ ratios of the $z = 6-9$ galaxies compared to the $z \sim 0$ galaxies. Thus the lower PDR covering fraction could be an origin of the high [O III]/[C II] ratio of high-redshift galaxies. The low PDR covering fraction may be due to compact sizes of galaxies or outflow, consistent with observational evidence of higher outflow velocity in higher redshift galaxies (Sugahara et al. 2017, 2019). These low-$C_{\rm PDR}$ galaxies may allow a significant escape of Lyman continuum photons like a density-bounded nebula (Figure 15(c); Nakajima & Ouchi 2014), and can be important contributors for the cosmic reionization.
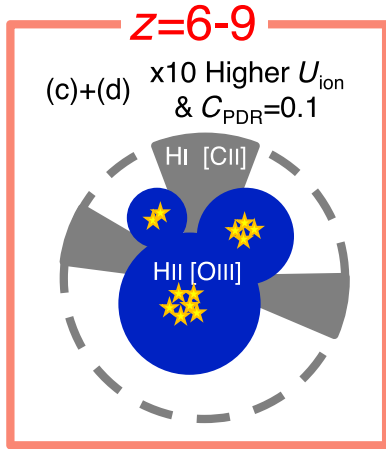
Figure 16. Same as Figure 15, but for a case of the combination of case (b) and (c); ×10 higher U_{ion} and $C_{PDR} = 0.1$.

(F) CMB attenuation effect. At $z = 6$–9, the CMB radiation affects FIR emission lines from galaxies, because the CMB temperature is around 20–30 K, sometimes comparable to excitation temperatures of the emission lines (e.g., Da Cunha et al. 2013; González-López et al. 2014; Pallottini et al. 2015, 2017b; Vallini et al. 2015; Lagache et al. 2018). The CMB effect does not have a significant impact on emission from H II regions (e.g., [O III]) due to its high excitation temperature, but becomes important for emission from PDRs, such as [C II] in diffuse PDRs. The high temperature of the CMB can heat the C^+ gas, while the CMB represents a strong background. As a result the [C II] emission appears to be weaker, so called the CMB attenuation. Recent calculations by Lagache et al. (2018) show that [C II] emission is significantly attenuated by the CMB (see also González-López et al. 2014). However, as discussed in Laporte et al. (2019), the maximum effect of the CMB attenuation is ~0.5 dex. Thus the CMB attenuation effect explains the 0.3–0.5 dex lower $L_{[C II]}$/SFR ratio of a part of the [C II] detected galaxies, but cannot explain the >1.0 dex lower ratio of the [C II] undetected galaxies at $z = 6$–9.

(G) Spatially extended [C II] halo. Fujimoto et al. (2019) detect spatially extended [C II] halos around galaxies at $z = 5$–7. Such [C II] halos could be missed in the flux measurements, resulting in the lower $L_{[C II]}$/SFR ratios of the $z = 6$–9 galaxies. However, we use the 2″-radius apertures for the flux measurements, which cover the total flux of the [C II] halo. In addition, this effect is not enough to explain the low $L_{[C II]}$/SFR ratios in other studies. For example, if the [C II] emission flux is measured in a ~0″.7 diameter aperture, comparable to beam sizes in Inoue et al. (2016) and Laporte et al. (2019), the total flux is underestimated only up to ~0.6 dex, assuming the radial profile of the [C II] halo in Fujimoto et al. (2019). Thus the extended [C II] halo cannot explain the low $L_{[C II]}$/SFR ratios of the $z = 6$–9 galaxies.

(H) Inclination effect. Kohandel et al. (2019) suggest that inclination effects are responsible for some of the non-detections of [C II] emission in $z > 6$ galaxies. Mock ALMA simulations in Kohandel et al. (2019) show that [C II] is detected at >5σ when seen face-on, while in the
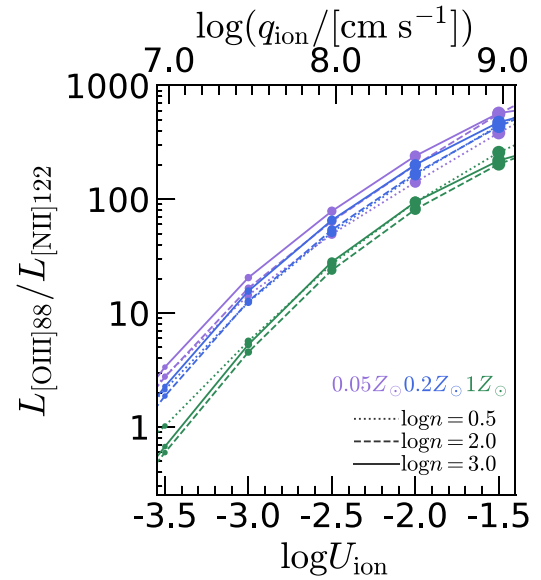
Figure 17. Cloudy calculation results for $L_{[O III]}/L_{[NII]}$ ratios as a function of the ionization parameter. The purple, blue, and green lines are results for metallicities of $Z = 0.05 Z_\odot$, $0.2 Z_\odot$, and $1.0 Z_\odot$, respectively. The dotted, dashed, and solid lines correspond to densities of $\log(n_H/[cm^{-3}]) = 0.5$, 2.0, and 3.0, respectively. The larger circles indicate higher ionization parameters, from $\log U_{ion} = -4.0$ to -0.5 with a step size of 0.5. The solar N/O abundance ratio is assumed.

edge-on case, it remains undetected because the larger intrinsic FWHM (~600 km s^{-1}) pushes the line peak flux below the detection limit. However, in this case, the [O III] emission line is also difficult to be detected, resulting no significant change in the [O III]/[C II] ratio. In addition, the observed FWHMs of the emission lines are 200–400 km s^{-1}, not as large as 600 km s^{-1} predicted in Kohandel et al. (2019). Thus the inclination effect cannot explain the high [O III]/[C II] ratio of $z = 6$–9 galaxies.

Based on these discussions, we conclude that (A) higher ionization parameter or (E) lower PDR covering fraction can explain the properties of the $z = 6$–9 galaxies including the high [O III]/[C II] ratios and low $L_{[C II]}$/SFR ratios. Figure 15 illustrates these cases. Compared to the $z \sim 0$ galaxies (case (a)), we need the ×100 higher ionization parameter (case (b)), or very low PDR covering fraction ($C_{PDR} = 0$) like a density-bounded nebula (case (c)). The middle of these two cases, i.e., × ~ 10 higher U_{ion} and $C_{PDR} \sim 0.1$, is also possible (Figure 16). We find that (C) higher density, (D) lower C/O ratio, and (F) CMB attenuation effect can reproduce only a part of the $z = 6$–9 galaxies, but these effects cannot explain all of the $z = 6$–9 galaxies with [O III] and [C II] observations by itself. The combination of two of these effects can reproduce the observed properties of the $z = 6$–9 galaxies.

6.2. [O III]/[N II] Ratios and Ionization Parameters

Figure 17 shows the [O III]88 μm/[N II]122 μm ratio as a function of the ionization parameter from our Cloudy calculations. Since the critical densities of [N II]122 μm and [O III]88 μm are similar (310 and 510 cm^{-3}, respectively), the [O III]/[N II] ratio is not sensitive to the electron density, but sensitive to the ionization parameter, due to the different ionization potential between O^{2+} and N^+. Figure 17 also
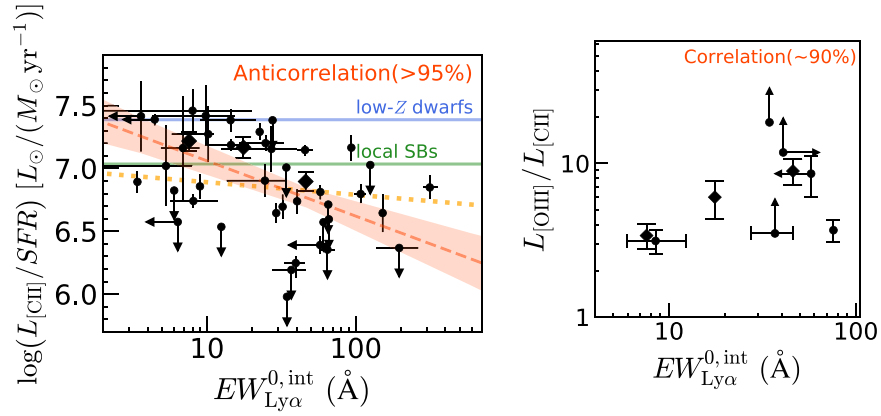
Figure 18. (Left panel) $L_{[\mathrm{C\,II}]}/\mathrm{SFR}$ as a function of the rest-frame Lyα EW. The black diamonds represent our targets at $z \sim 6$, and the black circles are other $z = 5$–9 galaxies in the literature (see Table 2). We find an anticorrelation between $L_{[\mathrm{C\,II}]}/\mathrm{SFR}$ and the rest-frame intrinsic Lyα EW, $\mathrm{EW}_{\mathrm{Ly}\alpha}^{0,\mathrm{int}}$, at the $>95\%$ significance level. The red dashed line and the shaded regions are the best-fit relation and its uncertainty. The blue and green horizontal lines show the $L_{[\mathrm{C\,II}]}/\mathrm{SFR}$ ratios for low-metallicity dwarf galaxies and local starburst galaxies in de Looze et al. (2014), respectively, for SFR $= 10\ M_\odot\ \mathrm{yr}^{-1}$. The orange dotted line is a fitting function in Schaerer et al. (2020). The rest-frame intrinsic Lyα EW, $\mathrm{EW}_{\mathrm{Ly}\alpha}^{0,\mathrm{int}}$ is calculated from the observed rest-frame Lyα EW following Equations (13)-(17) in Harikane et al. (2018b). (Right panel) [O III]/[C II] ratios as a function of the rest-frame Lyα EW. The black diamonds represent our targets at $z \sim 6$, and the black circles are other $z = 6$–9 galaxies in the literature (see Table 2). We identify a correlation between $L_{[\mathrm{O\,III}]}/L_{[\mathrm{C\,II}]}$ and $\mathrm{EW}_{\mathrm{Ly}\alpha}^{0,\mathrm{int}}$ at the $\sim 90\%$ significance level.

indicates that the [O III]/[N II] ratio becomes lower with higher metallicity due to fewer high-energy photons ionizing O^+ to O^{2+}. The N/O abundance ratio is assumed to be the solar abundance ratio. This assumption is reasonable as long as we are focusing on galaxies with $Z < 0.23\ Z_\odot$ (Kewley & Dopita 2002). Here we discuss whether the non-detections of [N II] in our targets are consistent with high U_{ion} or low C_{PDR} scenarios suggested by the high [O III]/[C II] ratio in Section 6.1. The observed [O III]/[N II] ratios are >5.8, >3.2, and >13.8 for J1211-0118, J0235-0532, and J0217-0208, respectively, corresponding to ionization parameters of $\log U_{\mathrm{ion}} > -3.1$. This is consistent with the high U_{ion} scenario ($\log U_{\mathrm{ion}} > -3$), and the low C_{PDR} scenario with fixed $U_{\mathrm{ion}} = -3$. Note that the [O III]/[N II] ratio also depends on the excitation temperature, because the [O III]88 μm line is the lower transition ($^3P_1 \rightarrow {}^3P_0$)while the [N II]122 μm line is the upper transition ($^3P_2 \rightarrow {}^3P_1$). Nonetheless, recent ALMA observations report weak [N II]205 μm ($^3P_1 \rightarrow {}^3P_0$) lines in LBGs at $z \sim 5$ probably due to high ionization parameters (Pavesi et al. 2016, 2019), consistent with our results.

6.3. Correlations with Lyα and Physical Interpretations

Harikane et al. (2018b) report the anticorrelation between the $L_{[\mathrm{C\,II}]}/\mathrm{SFR}$ ratio and the Lyα EW, indicating the [C II] deficit in LAEs. Our targets show a good anticorrelation with $(L_{[\mathrm{C\,II}]}/\mathrm{SFR}, \mathrm{EW}_{\mathrm{Ly}\alpha}^0) = (1.6 \times 10^7, 6.9)$, $(1.5 \times 10^7, 15)$, and $(0.8 \times 10^7, 41)$ in units of $(L_\odot/(M_\odot\ \mathrm{yr}^{-1}),\ \text{Å})$ for J1211-0118, J0217-0208, and J0235-0532, respectively. Including the results of our targets and the literature, we find that the anticorrelation holds with the 99.6% significance level with the Kendalls tau test (see the left panel of Figure 18). In the left panel of Figure 18, we also plot the following power-law function:

$$\log(L_{[\mathrm{C\,II}]}/\mathrm{SFR}) = -0.44 \times \log \mathrm{EW}_{\mathrm{Ly}\alpha}^{0,\mathrm{int}} + 7.5. \qquad (9)$$

In order to investigate whether this anticorrelation is made by a selection effect in which high $\mathrm{EW}_{\mathrm{Ly}\alpha}^0$ galaxies tend to be less luminous (less massive) galaxies, we calculate median SFRs of galaxies in $\mathrm{EW}_{\mathrm{Ly}\alpha}^{0,\mathrm{int}}$ bins. The calculated median SFRs are 21, 26,

and 18 $M_\odot\ \mathrm{yr}^{-1}$ for $\mathrm{EW}_{\mathrm{Ly}\alpha}^{0,\mathrm{int}} < 10$ Å, 10 Å $< \mathrm{EW}_{\mathrm{Ly}\alpha}^{0,\mathrm{int}} < 50$ Å, and 50 Å $< \mathrm{EW}_{\mathrm{Ly}\alpha}^{0,\mathrm{int}}$, respectively. Because the SFR values are not significantly different, the anticorrelation would not be explained by the selection effect.

Recently, Schaerer et al. (2020) studied the $L_{[\mathrm{C\,II}]}/\mathrm{SFR}$–$\mathrm{EW}_{\mathrm{Ly}\alpha}^0$ relation using the ALPINE sample, and reported a weaker dependence of $L_{[\mathrm{C\,II}]}/\mathrm{SFR}$ on $\mathrm{EW}_{\mathrm{Ly}\alpha}^0$ with a slope of -0.11 in Equation (9) compared to our result. They discussed that the difference between their result and our result can be explained by the sample difference, their use of a single IMF, a consistent use of calibrated SFRs (no SED-based SFRs) following Matthee et al. (2019), and/or an adoption of conservative line widths to derive $L_{[\mathrm{C\,II}]}$ upper limits. Regarding the IMF, all of the SFRs used in this study are based on the Chabrier (2003) IMF and corrected for the IMF differences. To check whether the difference in the $L_{[\mathrm{C\,II}]}/\mathrm{SFR}$–$\mathrm{EW}_{\mathrm{Ly}\alpha}^0$ relations is due to the methods of estimating SFRs or deriving $L_{[\mathrm{C\,II}]}$ upper limits, we calculate the significance level of the anticorrelation from our sample in two cases of using SFRs in Matthee et al. (2019), and excluding upper limit data. We find that the anticorrelation is significant with the 99.5% and 99.4% significance levels (with slopes of -0.50 and -0.36 in Equation (9)) in these two cases, respectively, indicating that the difference of the method cannot explain the difference in the $L_{[\mathrm{C\,II}]}/\mathrm{SFR}$–$\mathrm{EW}_{\mathrm{Ly}\alpha}^0$ relations. We also calculate the significance using our sample without correction for IGM absorption in Harikane et al. (2018b), and find that the anticorrelation still holds at the 95% level (with a slope of -0.28). These results indicate that the difference of the $L_{[\mathrm{C\,II}]}/\mathrm{SFR}$–$\mathrm{EW}_{\mathrm{Ly}\alpha}^0$ relation in this study and Schaerer et al. (2020) is due to the sample difference. One possible explanation is a difference of redshifts in the samples. Our galaxies are mainly at $z > 6$, while the ALPINE sample in Schaerer et al. (2020) is based on galaxies at $z = 4$–6. The other possible explanation is a difference of specific SFRs. Our galaxy sample contains all of the results reported, while the ALPINE sample is selected to be located on the star formation main sequence, which could miss galaxies with high specific SFRs such as LAEs (Ono et al. 2010; Hagen et al. 2016; Harikane et al. 2018b).

The right panel of Figure 18 shows the [O III]/[C II] ratios as a function of the Lyα EW. We find that galaxies with higher $EW_{Ly\alpha}^{0,int}$ tend to have higher [O III]/[C II] ratios at the ∼90% significance level (see also Hashimoto et al. 2019a). As discussed in Section 6.1, high [O III]/[C II] ratios would be due to high ionization parameters or low PDR covering fraction. In the high ionization parameter case, the intense radiation field would ionize C^+ and neutral hydrogen in PDRs, decreasing the [C II] emissivity and HI column density, and increasing the transmission of Lyα. In the low PDR covering fraction case, Lyα photons directly escape from H II regions that are not covered by PDRs. Thus, the origin of the [C II] deficit in LAEs would be the high ionization parameter or low PDR covering fraction.

The low PDR covering fraction would also enhance the Lyman continuum photon escape from galaxies at the reionization epoch. Indeed, recently Wang et al. (2019) report that $z \sim 0$ galaxies with weak [S II] emission are Lyman continuum leakers. Since the ionization potential of S II is 10.4 eV, less than that of H II (13.6 eV), most of the [S II] emission come from PDRs. Thus weak [S II] emission would be signposts of the low PDR covering fraction, resulting the Lyman continuum leakage. Because the ionization potential of C II is 11.3 eV, less than 13.6 eV, the weak [C II] emission will be also signposts of the Lyman continuum leakage. Therefore, the $z = 6$–9 galaxies with low $L_{[C II]}$/SFR (and high $L_{[O III]}/L_{[C II]}$) would be Lyman continuum leakers, significantly contributing to reionization.

7. Summary

In this paper, we present our new ALMA observations targeting three LBGs at $z \sim 6$, J1211-0118, J0235-0532, and J0217-0208, which are identified in the Subaru/HSC survey, and are already spectroscopically confirmed with Lyα. In conjunction with the previous ALMA observations for $z > 5$ galaxies, we study [O III]88 μm, [C II]158 μm, [N II]122 μm, and dust-continuum emission, and examine their relations with SFRs and rest-UV properties such as the UV slope β and the Lyα EWs. We then discuss the physical origins of the observed properties based on the model calculations with Cloudy. Our major findings are summarized as below.

1. We detect [O III] and [C II] emission lines from all of our targets at the 4.3–11.8σ significance levels. The redshifts derived from the [O III] and [C II] lines are consistent within 1σ uncertainties, and Lyα emission lines are redshifted from the [O III] and [C II] redshifts by $\Delta v_{Ly\alpha} \simeq 40$–200 km s^{-1}. The [N II] emission are not detected at $>3\sigma$ in our targets.

2. The [O III] luminosities of our targets are comparable to or higher than the $L_{[O III]}$–SFR relation of $z \sim 0$ low-metallicity dwarf galaxies. The [C II] luminosities are lower than those of the dwarf galaxies, and comparable to the local starburst galaxies. As a result, our galaxies show ∼10 times higher [O III]/[C II] ratios than local galaxies, similar to other $z = 6$–9 galaxies in the literature.

3. In J1211-0118 and J0217-0208, the [C II] emission are spatially well resolved, and show velocity gradients of $\Delta v_{obs} \sim 220$–250 km s^{-1}. The ratios of the velocity gradient to the velocity dispersion are $\Delta v_{obs}/2\sigma_{tot} > 0.4$, indicating that J1211-0118 and J0217-0208 are consistent with rotation supported systems.

4. We identify dust-continuum emission at 120 μm and 160 μm in J1211-0118 and J0217-0208, but not in J0235-0532. We fit the observed continuum fluxes and upper limits with the modified blackbody, and obtain the IR luminosities of $L_{IR} \sim 10^{11} L_\odot$, and the dust temperatures of $T_{dust} \sim 30$–40 K for J1211-0118 and J0217-0208. We also obtain the upper limit of $L_{IR} < 2.5 \times 10^{11} L_\odot$ with $T_{dust} < 50$ K for J0235-0532.

5. J1211-0118 follows the Calzetti IRX–β_{UV} relation, and the upper limit of J0235-0532 is consistent with both the Calzetti, Takeuchi, and SMC relations. The IRX value of J0217-0208 is lower than the SMC IRX–β relation, which would be due to the geometry effect, AGN activity, or the high molecular gas fraction.

6. Based on the Cloudy calculations, we discuss the physical origins of the high [O III]/[C II] ratios and low $L_{[C II]}$/SFR ratios of the $z = 6$–9 galaxies compared to the $z \sim 0$ galaxies. We find that the properties of the $z = 6$–9 galaxies can be explained by $\times 10$–100 higher ionization parameters or low PDR covering fractions of 0%–10% like a density-bounded nebula, possibly due to the young stellar populations, compact sizes of the $z = 6$–9 galaxies, or outflow, consistent with our [N II] observations. The low PDR covering fraction would enhancing the Lyα, Lyman continuum, and C^+ ionizing photon escapes from galaxies. Higher hydrogen density, lower C/O ratio, and the CMB attenuation effect can reproduce a part of the $z = 6$–9 galaxies, but not all of the $z = 6$–9 galaxies with [O III] and [C II] observations by itself, and the combination of these effects is needed.

7. Including our new observations, we find the antic-orrelation between $L_{[C II]}$/SFR and $EW_{Ly\alpha}^{0,int}$ at the $>95\%$ significance level. We also identify the correlation between the [O III]/[C II] ratio and the Lyα EW at the ∼90% significance level. These relations indicate that the origin of the [C II] deficit in LAEs would be the high ionization parameters or low PDR covering fractions, which make the Lyα and Lyman continuum photons escape easier.

ORCID iDs

Yuichi Harikane ⦾ https://orcid.org/0000-0002-6047-430X
Masami Ouchi ⦾ https://orcid.org/0000-0002-1049-6658
Yoichi Tamura ⦾ https://orcid.org/0000-0003-4807-8117
Seiji Fujimoto ⦾ https://orcid.org/0000-0001-7201-5066
Tohru Nagao ⦾ https://orcid.org/0000-0002-7402-5441
Ken-ichi Tadaki ⦾ https://orcid.org/0000-0001-9728-8909
Takashi Kojima ⦾ https://orcid.org/0000-0001-5780-1886
Andrea Ferrara ⦾ https://orcid.org/0000-0002-9400-7312
Takuya Hashimoto ⦾ https://orcid.org/0000-0002-0898-4038
Kotaro Kohno ⦾ https://orcid.org/0000-0002-4052-2394
Yuichi Matsuda ⦾ https://orcid.org/0000-0003-1747-2891
Yuma Sugahara ⦾ https://orcid.org/0000-0001-6958-7856
Livia Vallini ⦾ https://orcid.org/0000-0002-3258-3672

References

Abel, N. P., Ferland, G. J., Shaw, G., & van Hoof, P. A. M. 2005, ApJS, 161, 65
Aihara, H., Arimoto, N., Armstrong, R., et al. 2018, PASJ, 70, S4
Arata, S., Yajima, H., Nagamine, K., Abe, M., & Khochfar, S. 2020, arXiv:2001.01853
Bakx, T. J. L. C., Tamura, Y., Hashimoto, T., et al. 2020, MNRAS, 493, 4294
Bañados, E., Novak, M., Neeleman, M., et al. 2019, ApJL, 881, L23
Barisic, I., Faisst, A. L., Capak, P. L., et al. 2017, ApJ, 845, 41
Behrens, C., Pallottini, A., Ferrara, A., Gallerani, S., & Vallini, L. 2018, MNRAS, 477, 552
Bouwens, R. J., Aravena, M., Decarli, R., et al. 2016, ApJ, 833, 72
Bradač, M., Garcia-Appadoo, D., Huang, K.-H., et al. 2017, ApJL, 836, L2
Calzetti, D., Armus, L., Bohlin, R. C., et al. 2000, ApJ, 533, 682
Capak, P. L., Carilli, C., Jones, G., et al. 2015, Natur, 522, 455
Carniani, S., Maiolino, R., Amorin, R., et al. 2018a, MNRAS, 478, 1170
Carniani, S., Maiolino, R., Pallottini, A., et al. 2017, A&A, 605, A42
Carniani, S., Maiolino, R., Smit, R., & Amorín, R. 2018b, ApJL, 854, L7
Chabrier, G. 2003, PASP, 115, 763
Cooke, R. J., Pettini, M., & Steidel, C. C. 2017, MNRAS, 467, 802
Cormier, D., Abel, N. P., Hony, S., et al. 2019, A&A, 626, A23
Cormier, D., Madden, S. C., Lebouteiller, V., et al. 2015, A&A, 578, A53
Cuby, J.-G., le Fèvre, O., McCracken, H., et al. 2003, A&A, 405, L19
Da Cunha, E., Groves, B., Walter, F., et al. 2013, ApJ, 766, 13
de Looze, I., Cormier, D., Lebouteiller, V., et al. 2014, A&A, 568, A62
Díaz-Santos, T., Armus, L., Charmandaris, V., et al. 2017, ApJ, 846, 32
Eldridge, J. J., Stanway, E. R., Xiao, L., et al. 2017, PASA, 34, e058
Erb, D. K., Steidel, C. C., Trainor, R. F., et al. 2014, ApJ, 795, 33
Faisst, A. L., Capak, P., Hsieh, B. C., et al. 2016, ApJ, 821, 122
Faisst, A. L., Capak, P. L., Yan, L., et al. 2017, ApJ, 847, 21
Ferland, G. J., Chatzikos, M., Guzmán, F., et al. 2017, RMxAA, 53, 385
Ferland, G. J., Korista, K. T., Verner, D. A., et al. 1998, PASP, 110, 761
Ferrara, A., Hirashita, H., Ouchi, M., & Fujimoto, S. 2017, MNRAS, 471, 5018
Ferrara, A., Vallini, L., Pallottini, A., et al. 2019, MNRAS, 489, 1
Finkelstein, S. L., Papovich, C., Dickinson, M., et al. 2013, Natur, 502, 524
Förster Schreiber, N. M., Genzel, R., Bouché, N., et al. 2009, ApJ, 706, 1364
Fudamoto, Y., Oesch, P. A., Schinnerer, E., et al. 2017, MNRAS, 472, 483
Fujimoto, S., Ouchi, M., Ferrara, A., et al. 2019, ApJ, 887, 107
Furusawa, H., Kashikawa, N., Kobayashi, M. A. R., et al. 2016, ApJ, 822, 46
Gallerani, S., Maiolino, R., Juarez, Y., et al. 2010, A&A, 523, A85
González-López, J., Riechers, D. A., Decarli, R., et al. 2014, ApJ, 784, 99
Groves, B. A., Dopita, M. A., & Sutherland, R. S. 2004, ApJS, 153, 75
Hagen, A., Zeimann, G. R., Behrens, C., et al. 2016, ApJ, 817, 79
Harikane, Y., Ouchi, M., Ono, Y., et al. 2018a, PASJ, 70, S11
Harikane, Y., Ouchi, M., Shibuya, T., et al. 2018b, ApJ, 859, 84
Hashimoto, T., Inoue, A. K., Mawatari, K., et al. 2019a, PASJ, 71, 71
Hashimoto, T., Inoue, A. K., Tamura, Y., et al. 2019b, PASJ, 71, 109
Hashimoto, T., Laporte, N., Mawatari, K., et al. 2018, Natur, 557, 392
Hashimoto, T., Ouchi, M., Shimasaku, K., et al. 2013, ApJ, 765, 70
Hildebrand, R. H. 1983, QJRAS, 24, 267
Hosokawa, T., & Inutsuka, S.-i. 2005, ApJ, 623, 917
Howell, J. H., Armus, L., Mazzarella, J. M., et al. 2010, ApJ, 715, 572
Hu, E. M., Cowie, L. L., McMahon, R. G., et al. 2002, ApJL, 568, L75
Inoue, A. K., Shimizu, I., Tamura, Y., et al. 2014, ApJL, 780, L18
Inoue, A. K., Tamura, Y., Matsuo, H., et al. 2016, Sci, 352, 1559
Kanekar, N., Wagg, J., Chary, R. R., & Carilli, C. L. 2013, ApJL, 771, L20
Kashino, D., Silverman, J. D., Sanders, D., et al. 2017, ApJ, 835, 88
Kaufman, M. J., Wolfire, M. G., & Hollenbach, D. J. 2006, ApJ, 644, 283
Kennicutt, R. C. J. 1998, ARA&A, 36, 189
Kewley, L. J., & Dopita, M. A. 2002, ApJS, 142, 35
Knudsen, K. K., Richard, J., Kneib, J.-P., et al. 2016, MNRAS, 462, L6
Knudsen, K. K., Watson, D., Frayer, D., et al. 2017, MNRAS, 466, 138
Kohandel, M., Pallottini, A., Ferrara, A., et al. 2019, MNRAS, 487, 3007
Konno, A., Ouchi, M., Nakajima, K., et al. 2016, ApJ, 823, 20
Koprowski, M. P., Coppin, K. E. K., Geach, J. E., et al. 2018, MNRAS, 479, 4355
Lagache, G., Cousin, M., & Chatzikos, M. 2018, A&A, 609, A130
Laporte, N., Ellis, R. S., Boone, F., et al. 2017a, ApJL, 837, L21
Laporte, N., Katz, H., Ellis, R. S., et al. 2019, MNRAS, 487, L81
Laporte, N., Nakajima, K., Ellis, R. S., et al. 2017b, ApJ, 851, 40
Madden, S. C., Rémy-Ruyer, A., Galametz, M., et al. 2013, PASP, 125, 600
Mainali, R., Zitrin, A., Stark, D. P., et al. 2018, MNRAS, 479, 1180
Maiolino, R., Carniani, S., Fontana, A., et al. 2015, MNRAS, 452, 54
Maiolino, R., & Mannucci, F. 2019, A&Ar, 27, 3
Maiolino, R., Nagao, T., Grazian, A., et al. 2008, A&A, 488, 463
Mallery, R. P., Mobasher, B., Capak, P., et al. 2012, ApJ, 760, 128
Mancini, M., Schneider, R., Graziani, L., et al. 2015, MNRAS, 451, L70
Marrone, D. P., Spilker, J. S., Hayward, C. C., et al. 2018, Natur, 553, 51
Matsuoka, Y., Iwasawa, K., Onoue, M., et al. 2018a, ApJS, 237, 5
Matsuoka, Y., Iwasawa, K., Onoue, M., et al. 2019, ApJ, 883, 183

Matsuoka, Y., Onoue, M., Kashikawa, N., et al. 2016, ApJ, 828, 26
Matsuoka, Y., Onoue, M., Kashikawa, N., et al. 2018b, PASJ, 70, S35
Matthee, J., Sobral, D., Boogaard, L. A., et al. 2019, ApJ, 881, 124
Matthee, J., Sobral, D., Boone, F., et al. 2017, ApJ, 851, 145
McLure, R. J., Dunlop, J. S., Cullen, F., et al. 2018, MNRAS, 476, 3991
McMullin, J. P., Waters, B., Schiebel, D., Young, W., & Golap, K. 2007, in
    ASP Conf. Ser. 376, Astronomical Data Analysis Software and Systems
    XVI, ed. R. A. Shaw, F. Hill, & D. J. Bell (San Francisco, CA: ASP), 127
Meurer, G. R., Heckman, T. M., & Calzetti, D. 1999, ApJ, 521, 64
Moriwaki, K., Yoshida, N., Shimizu, I., et al. 2018, MNRAS, 481, L84
Nagao, T., Maiolino, R., de Breuck, C., et al. 2012, A&A, 542, L34
Nagao, T., Maiolino, R., Marconi, A., & Matsuhara, H. 2011, A&A, 526, A149
Nakajima, K., & Ouchi, M. 2014, MNRAS, 442, 900
Oke, J. B., & Gunn, J. E. 1983, ApJ, 266, 713
Ono, Y., Ouchi, M., Harikane, Y., et al. 2018, PASJ, 70, S10
Ono, Y., Ouchi, M., Mobasher, B., et al. 2012, ApJ, 744, 83
Ono, Y., Ouchi, M., Shimasaku, K., et al. 2010, MNRAS, 402, 1580
Ota, K., Walter, F., Ohta, K., et al. 2014, ApJ, 792, 34
Ouchi, M., Ellis, R., Ono, Y., et al. 2013, ApJ, 778, 102
Pallottini, A., Ferrara, A., Bovino, S., et al. 2017a, MNRAS, 471, 4128
Pallottini, A., Ferrara, A., Decataldo, D., et al. 2019, MNRAS, 487, 1689
Pallottini, A., Ferrara, A., Gallerani, S., et al. 2017b, MNRAS, 465, 2540
Pallottini, A., Gallerani, S., Ferrara, A., et al. 2015, MNRAS, 453, 1898
Pavesi, R., Riechers, D. A., Capak, P. L., et al. 2016, ApJ, 832, 151
Pavesi, R., Riechers, D. A., Faisst, A. L., Stacey, G. J., & Capak, P. L. 2019,
    ApJ, 882, 168
Pentericci, L., Carniani, S., Castellano, M., et al. 2016, ApJL, 829, L11
Pettini, M., Kellogg, M., Steidel, C. C., et al. 1998, ApJ, 508, 539
Planck Collaboration, Ade, P. A. R., Aghanim, N., et al. 2016, A&A, 594, A13
Reddy, N. A., Oesch, P. A., Bouwens, R. J., et al. 2018, ApJ, 853, 56
Rémy-Ruyer, A., Madden, S. C., Galliano, F., et al. 2015, A&A, 582, A121
Roberts-Borsani, G. W., Bouwens, R. J., Oesch, P. A., et al. 2016, ApJ,
    823, 143
Salpeter, E. E. 1955, ApJ, 121, 161
Sanders, R. L., Shapley, A. E., Kriek, M., et al. 2016, ApJ, 816, 23
Saturni, F. G., Mancini, M., Pezzulli, E., & Tombesi, F. 2018, A&A,
    617, A131
Schaerer, D., Boone, F., Zamojski, M., et al. 2015, A&A, 574, A19

Schaerer, D., Ginolfi, M., Bethermin, M., et al. 2020, arXiv:2002.00979
Schlegel, D. J., Finkbeiner, D. P., & Davis, M. 1998, ApJ, 500, 525
Shibuya, T., Kashikawa, N., Ota, K., et al. 2012, ApJ, 752, 114
Shibuya, T., Ouchi, M., & Harikane, Y. 2015, ApJS, 219, 15
Shibuya, T., Ouchi, M., Harikane, Y., et al. 2018, PASJ, 70, S15
Shibuya, T., Ouchi, M., Nakajima, K., et al. 2014, ApJ, 788, 74
Shimakawa, R., Kodama, T., Steidel, C. C., et al. 2015, MNRAS, 451, 1284
Smit, R., Bouwens, R. J., Carniani, S., et al. 2018, Natur, 553, 7687
Sobral, D., & Matthee, J. 2019, A&A, 623, A157
Sobral, D., Matthee, J., Best, P., et al. 2017, MNRAS, 466, 1242
Sobral, D., Matthee, J., Darvish, B., et al. 2015, ApJ, 808, 139
Song, M., Finkelstein, S. L., Ashby, M. L. N., et al. 2016, ApJ, 825, 5
Stark, D. P., Ellis, R. S., Charlot, S., et al. 2017, MNRAS, 464, 469
Stark, D. P., Richard, J., Charlot, S., et al. 2015a, MNRAS, 450, 1846
Stark, D. P., Walth, G., Charlot, S., et al. 2015b, MNRAS, 454, 1393
Steidel, C. C., Strom, A. L., Pettini, M., et al. 2016, ApJ, 826, 159
Sugahara, Y., Ouchi, M., Harikane, Y., et al. 2019, ApJ, 886, 29
Sugahara, Y., Ouchi, M., Lin, L., et al. 2017, ApJ, 850, 51
Tadaki, K., Iono, D., Yun, M. S., et al. 2018, Natur, 560, 613
Tadaki, K.-i., Iono, D., Hatsukade, B., et al. 2019, ApJ, 876, 1
Takeuchi, T. T., Yuan, F.-T., Ikeyama, A., Murata, K. L., & Inoue, A. K. 2012,
    ApJ, 755, 144
Tamura, Y., Mawatari, K., Hashimoto, T., et al. 2019, ApJ, 874, 27
Toshikawa, J., Uchiyama, H., Kashikawa, N., et al. 2018, PASJ, 70, S12
Trainor, R. F., Strom, A. L., Steidel, C. C., & Rudie, G. C. 2016, ApJ, 832,
    171
Vallini, L., Ferrara, A., Pallottini, A., & Gallerani, S. 2017, MNRAS,
    467, 1300
Vallini, L., Gallerani, S., Ferrara, A., Pallottini, A., & Yue, B. 2015, ApJ,
    813, 36
Vanzella, E., Pentericci, L., Fontana, A., et al. 2011, ApJL, 730, L35
Walter, F., Riechers, D., Novak, M., et al. 2018, ApJL, 869, L22
Wang, B., Heckman, T. M., Leitherer, C., et al. 2019, ApJ, 885, 57
Watson, D., Christensen, L., Knudsen, K. K., et al. 2015, Natur, 519, 327
Willott, C. J., Carilli, C. L., Wagg, J., & Wang, R. 2015, ApJ, 807, 180
Willott, C. J., McLure, R. J., Hibon, P., et al. 2013, AJ, 145, 4
Wolfire, M. G., Hollenbach, D., & McKee, C. F. 2010, ApJ, 716, 1191
Yeh, S. C. C., & Matzner, C. D. 2012, ApJ, 757, 108